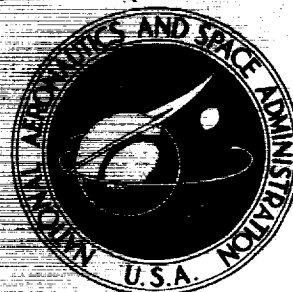


~~RESTRICTED DATA~~

~~ATOMIC ENERGY ACT OF 1954~~

NASA TECHNICAL MEMORANDUM



UB
NASA TM X-1422

(NASA-TM-X-1422) FEASIBILITY STUDY OF A
TUNGSTEN WATER-MODERATED NUCLEAR ROCKET.
3: FUEL ELEMENTS A.F. Lietzke (NASA)
Mar. 1968 84 p

N72-14699

CO/99 Unclass
40223

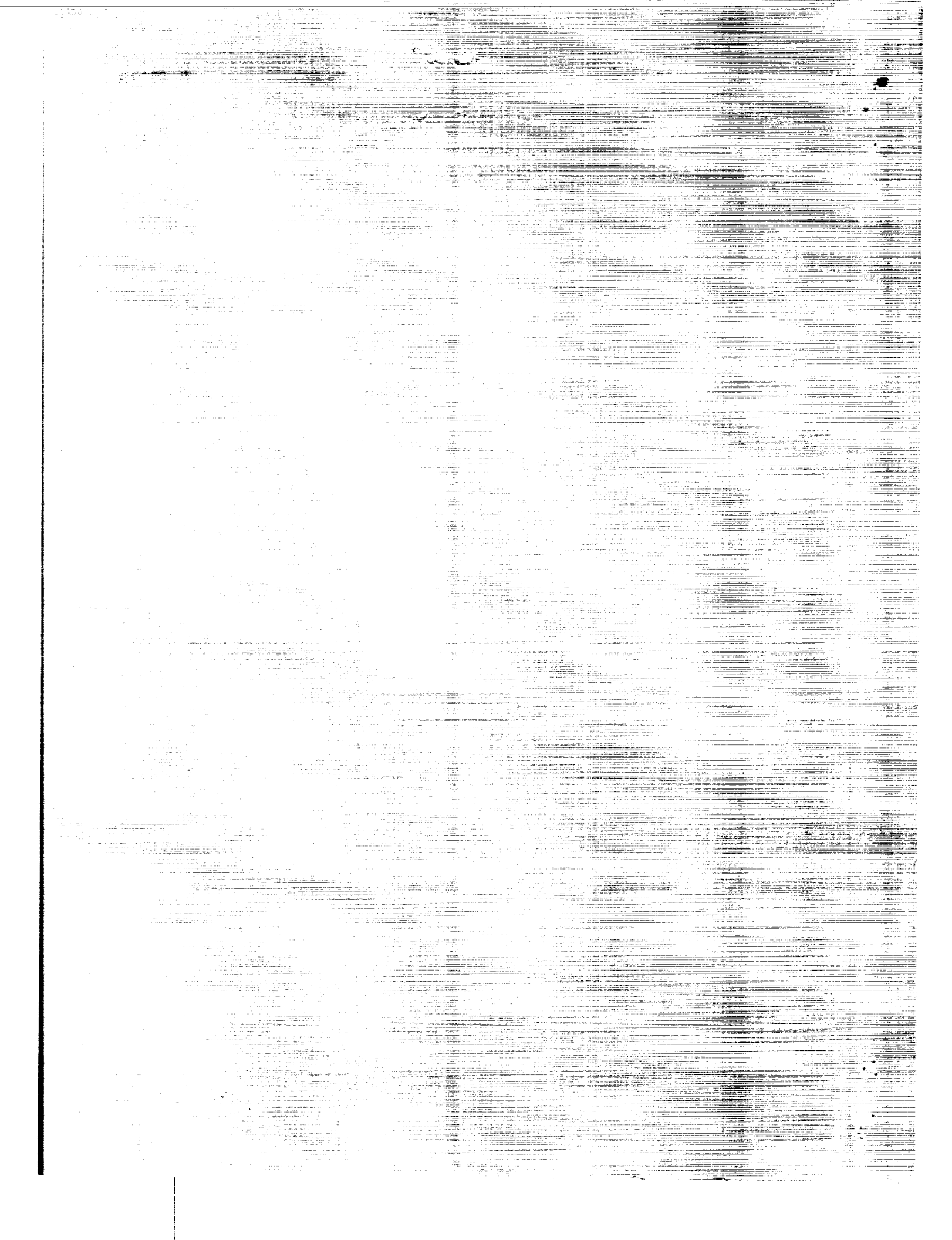
FF No. 602(D)	X 68-50432	
	(ACCESSION NUMBER)	(THRU)
	84	28
	(PAGES)	(CODE)
	(NASA CR OR TMX OR AD NUMBER)	(CATEGORY)
		22
AVAILABLE TO U.S. GOVERNMENT AGENCIES AND CONTRACTORS ONLY		

FEASIBILITY
WATER

III. FUEL

by A. F. Lietzke
Lewis Research Center
Cleveland, Ohio

NATIONAL AERONAUTICS AND SPACE ADMINISTRATION



~~CONFIDENTIAL~~

NASA TM X-1422

FEASIBILITY STUDY OF A TUNGSTEN WATER-
MODERATED NUCLEAR ROCKET

III. FUEL ELEMENTS

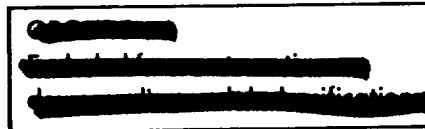
By A. F. Lietzke

Lewis Research Center
Cleveland, Ohio

Film supplement C-240 available on request

~~RESTRICTED DATA~~

ATOMIC ENERGY COMMISSION



TH [REDACTED]
[REDACTED]
[REDACTED]
[REDACTED]
[REDACTED]
[REDACTED]

[REDACTED]
[REDACTED]
[REDACTED]
[REDACTED]
[REDACTED]
[REDACTED]

NATIONAL AERONAUTICS AND SPACE ADMINISTRATION

~~CONFIDENTIAL~~

W
S
C

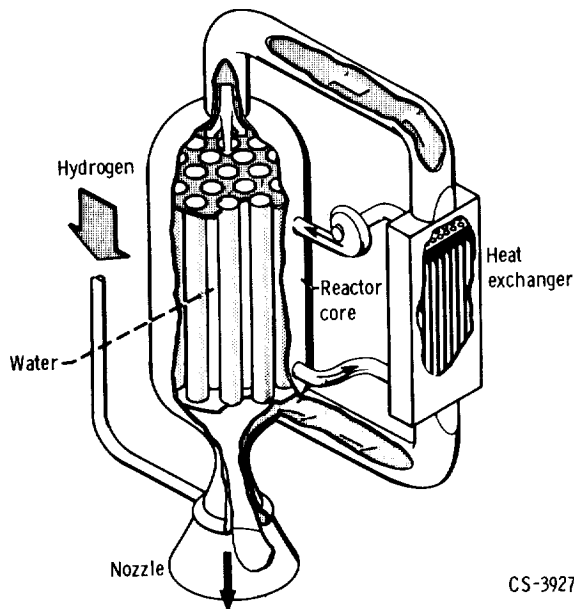
R

|

~~CONFIDENTIAL~~

PREFACE

The concept of a nuclear rocket system based on the use of a tungsten water-moderated reactor (TWMR) was originated at the Lewis Research Center. The TWMR is a thermal reactor that uses water as the moderator, uranium dioxide as the fuel, and tungsten enriched in tungsten 184 as the



CS-39273

fuel element structural material. As is common to all nuclear rocket systems, hydrogen is used as the propellant to maximize specific impulse. The reactor (see illustration) consists of a tank containing a number of pressure tubes that are attached to tube sheets at the inlet and outlet ends of the reactor. The pressure tubes contain the fuel elements. The space inside the tank between the tubes is filled with water, which serves both as the neutron moderator and as a coolant for the structure. Heat is generated in the water by neutrons and gamma rays and is also transferred to the water by heat leakage from the hot fuel elements, each of which is located in a pressure tube. The removal of heat is provided by pumping the water through the core and a heat exchanger in a closed loop. The water is regeneratively cooled in the heat exchanger by the hydrogen propellant, which flows from a

supply tank through the nozzle and heat exchanger into the core. As the hydrogen flows through the core pressure tubes and through the fuel elements, it is heated to a high temperature and is expanded out the nozzle to produce thrust.

The potential advantages of the concept lie in the following areas: The use of tungsten provides a high-temperature material with good thermal shock resistance, tensile and compressive strength, thermal conductivity, and resistance to corrosion by the hydrogen propellant. The properties of tungsten also permit the fabrication of fuel elements with very thin cross sections for good heat transfer. The use of water as the moderator provides a good coolant for the pressure vessel and structural members and reduces core size and weight over that obtained for most moderator materials. In this concept, the fuel element assemblies are structurally independent of each other and thus permit individual development of these assemblies.

A program was undertaken at Lewis to investigate the engineering feasibility and performance of the TWMR nuclear rocket system. The results of these investigations, which are summarized in part I (NASA Technical Memorandum X-1420) of this series of reports, are presented in detail in the other six parts of the series as follows: II. Fueled Materials (NASA Technical Memorandum X-1421); III. Fuel Elements (NASA Technical Memorandum X-1422); IV. Neutronics (NASA Technical Memorandum X-1423); V. Engine System (NASA Technical Memorandum X-1424); VI. Feed System and Rotating Machinery (NASA Technical Memorandum X-1425); VII. System Dynamics (NASA Technical Memorandum X-1426).

~~CONFIDENTIAL~~

CONTENTS

PRECEDING PAGE BLANK NOT FILMED.

	Page
SUMMARY	1
INTRODUCTION	2
DESIGN PARAMETERS	2
Length-to-Diameter Ratio	3
Interrelation of Operating Parameters	4
Fueled Material Composition	5
Fuel-Element Configurations	7
Concentric-cylinder configurations	7
Honeycomb configuration	8
Fuel-element arrangement	8
Reference-Design Parameter Values	8
DYNAMIC HEAD LIMITATIONS	9
Selection of a Substitute Material	10
Room-temperature flow tests	11
Hot-flow tests	12
Choice of substitute material	12
Concentric-Cylinder-Element Tests	12
Room-temperature flow tests	13
Hot-flow tests	14
Dynamic Head Limitations	16
THERMAL STRESSES IN HONEYCOMB FUEL ELEMENT	16
Temperature Distribution	17
Local temperature gradients	18
Radial temperature profile	22
Thermal Stress Tests	26
Thermal Stress Results	28
SUPPORT STRUCTURES	28
Axial Support Tests	29
Mechanical attachment evaluation	30
Metallurgical attachment evaluation	31
Results of Axial Supports	32
Lateral Support Evaluation	33
Thermal expansion evaluation	33
Lateral Vibration Evaluation	35
Determination of static spring constant	35

~~CONFIDENTIAL~~

Determination of dynamic spring constant	36
Damping evaluation	39
Clearance tests	41
Lateral Support Results	41
APPENDIXES	
A - SYMBOLS	43
B - AXIAL PROPELLANT TEMPERATURE DISTRIBUTION	45
C - REACTOR CORE PRESSURE DROP	48
D - APPARATUS AND PROCEDURE FOR ROOM-TEMPERATURE FLOW TESTS	50
E - APPARATUS AND PROCEDURE FOR HOT-FLOW TESTS	53
F - CALCULATION OF EXPERIMENTALLY INDUCED TEMPERATURE PROFILE	55
REFERENCES	58

~~CONFIDENTIAL~~

FEASIBILITY STUDY OF A TUNGSTEN WATER- MODERATED NUCLEAR ROCKET

III. FUEL ELEMENTS (U)

by A. F. Lietzke

Lewis Research Center

SUMMARY

A feasibility study of a water-moderated reactor using tungsten as the fuel element material was conducted at the Lewis Research Center. The investigation was initiated because of the potential application of this reactor concept to nuclear propulsion in space. This report presents the results of that part of the study associated with the fuel elements for this reactor.

Temperature, pressure, and flow rate parameters were studied to determine their effect on fuel-element operating conditions and dimensional requirements. Variations in fuel-element material composition and fueled material thickness were also considered. Specific fuel-element configurations were selected as a result of the study and experiments conducted to determine aerodynamic load limitations and behavior under thermal gradients. Because of the brittle nature of tungsten at low temperature, vibration tests were conducted on fuel-element support structures.

Experiments were conducted on concentric cylinder and honeycomb fuel-element configurations for a reference reactor. The concentric-cylinder fuel-element configuration was marginal for the dynamic head at the reference-design conditions unless many supports for the cylinders are incorporated into the design. The honeycomb fuel-element configuration is not dynamic-head limited because of the inherent rigidity of this geometry. Thermal stresses in a honeycomb presented no serious problem for the temperature gradients expected.

Two methods of supporting the fuel-element stages were investigated experimentally at temperature. These consisted of a pin-tab mechanical attachment and a metallurgically bonded attachment. Both designs proved to be suitable for the axial loads of the reference design. The pin-tab attachment failed under test as the result of creep, and a slight modification would be required to reduce the stress level.

A lateral fuel-element support consisting of a thin tungsten sheet in the form of a corrugated ring met all the requirements for temperature, thermal expansion, heat transfer, and dynamic characteristics.

~~CONFIDENTIAL~~

~~CONFIDENTIAL~~

INTRODUCTION

A water-moderated reactor using tungsten as the fuel-element structural material was investigated at the Lewis Research Center. The investigation was initiated to explore the feasibility of this concept because of its potential application to nuclear rocket propulsion in space. This concept is described in the preface and is discussed briefly in references 1 and 2.

As part of the investigation of this concept, various fuel-element studies were conducted. Temperature, pressure, and flow-rate parameters were investigated to determine their effect on fuel-element operating conditions and dimensional requirements. Variations in fuel-element material composition and fueled material thickness were also considered. The capabilities of tungsten fuel elements were, however, unknown. Therefore, specific fuel-element configurations were selected and experiments were conducted to determine aerodynamic load limitations and behavior under thermal gradients. Because of the brittle nature of tungsten at low temperature, vibration tests were conducted on fuel-element support structures.

Certain goals were established early in the program as a basis for the work. High-temperature fuel-element operation is essential if the specific impulse potential of the nuclear rocket is to be realized. The nominal fuel-element operating temperature was chosen to be 5000°R (2780°K). Although no specific space mission has been defined, the operating time is assumed to be short (approximately 1 hr) which is consistent with high-thrust propulsion and small-gravity losses. To allow for development testing, however, the total operating time was set at 10 hours. These 10 hours of operation will include a number of restarts. Again to provide for development testing, the number of thermal cycles for a design goal was chosen to be 25. Some fuel loss during operation can be tolerated, but to keep the excess reactivity necessary to compensate for fuel loss in line with other reactivity requirements, the allowable fuel loss was taken to be less than 1 percent.

This report presents the results of the studies conducted on fuel elements for the tungsten water-moderated reactor during the course of the concept investigation. Other reports concurrent with this report discuss other phases of this investigation, as outlined in the preface. The studies reported herein were the results of a group effort at the Lewis Research Center. Members of the staff who contributed substantially to this effort include Jack G. Slaby, Louis Gedeon, Roger L. Smith, Byron L. Siegel, William F. Mattson, Henry F. Kacher, and William L. Maag.

DESIGN PARAMETERS

The fuel elements in a rocket reactor serve to contain the fissionable fuel and to transfer the heat energy from the fission process to the propellant. The designer has

~~CONFIDENTIAL~~

various parameters under his control which should be selected to accomplish these functions most effectively. The purpose of this section is to discuss the selection of proper values for these parameters and the specific fuel-element configurations which might best incorporate these values for the tungsten water-moderated rocket reactor concept. A reference design, described in detail in reference 3, was carried along with the overall feasibility study in order to coordinate the many aspects of the program. The design values used in this reference design that are pertinent to the fuel elements are pointed out in this section. These values are not intended to represent optimum values since they were selected prior to the completion of the program and without a particular planned nuclear rocket mission.

Length to Diameter Ratio of Flow Passage

The specific impulse of any thermal rocket increases directly with the square root of the propellant temperature. If the temperature is sufficiently high, an additional benefit is derived from dissociation of the hydrogen propellant. It is desirable, therefore, to achieve maximum practical reactor outlet gas temperature.

In order to achieve maximum propellant temperature, the fuel elements must operate at the maximum temperature consistent with the materials of construction, and the heat-transfer flow passage must have a length to diameter ratio large enough so that the coolant temperature approaches the fuel-element surface temperature. The smallest length to diameter ratio is attained when the entire fuel element operates at the maximum allowable temperature. The variation of propellant temperature with length is derived in appendix B for constant surface temperature. The derivation results in an equation presented in terms of dimensionless quantities. The variation of propellant-to surface-temperature ratio with axial position resulting from this equation is shown in figure 1 for Reynolds numbers of 10 000, 20 000, and 60 000. The ratio of surface to propellant inlet temperature, T_s/T_i , used in figure 1 is 16.67 which is the approximate value of interest for this concept. The temperature ratio is low as the gas enters the reactor, but increases with l/D as shown in the figure. In order for the propellant temperature to approach the fuel-element surface temperature within 10 percent, it is apparent from figure 1 that a flow passage with a length to diameter ratio of 240 or greater is required. Thus, for example a reactor 36-inches-long (91 cm) requires an equivalent diameter of 0.15 inch (3.81 mm) at a Reynolds number of 10 000 and 0.10 inch (2.54 mm) at a Reynolds number of 60 000. Actually, slightly larger length to diameter ratios than shown here will be required because axial power distributions corresponding to constant surface temperature may not be practical from a reactor physics viewpoint. The reference design of reference 3 has a heated length of 39 inches (99 cm). The equivalent diameter of interest for the reference design is therefore approximately 0.125 inch (3.18 mm).

Interrelation of Operating Parameters

Basic operating parameters which influence reactor design, in addition to temperature, are the mass velocity and the pressure level. These in turn affect other parameters which define the conditions under which the reactor must operate. The Reynolds number is affected by the mass velocity G , the flow rate per unit flow area. The mass velocity is most significant because, with a fixed outlet temperature, it determines the power or thrust from a given flow area reactor. As the mass velocity is increased, the thrust increases, but the Reynolds number, core pressure drop, and outlet Mach number also increase.

The core pressure drop for continuous smooth passages is derived in appendix C. A more detailed calculation of pressure drop for the reference design is given in reference 3. The outlet Mach number M_o , also a function of mass velocity, can be obtained from the continuity equation by writing the velocity in terms of Mach number and the density in terms of total temperature and pressure, to yield

$$G = M_o P_o \left(1 + \frac{\gamma - 1}{2} M_o^2 \right)^{1+\gamma/2(1-\gamma)} \sqrt{\frac{\gamma g}{RT_o}}$$

All symbols are defined in appendix A.

A measure of the aerodynamic load acting on the fuel elements is the dynamic head. If M_o as a function of G is known, the dynamic head can be determined from

$$\left(\frac{\rho v^2}{2g} \right)_o = \frac{P_o M_o^{2\gamma}}{2 \left(1 + \frac{\gamma - 1}{2} M_o^2 \right)^{\gamma/\gamma-1}}$$

Core pressure drop and outlet Mach number are plotted against mass velocity for several chamber pressures in figure 2. The variation of dynamic head at the reactor outlet is also shown. The curves of figure 2 were calculated by using an inlet temperature T_i of 300°R (167°K), an outlet temperature T_o of 4500°R (2500°K), and a surface temperature T_s of 5000°R (2780°K). As the mass velocity is increased, the thrust increases. (The thrust per unit flow area is the product of mass velocity and specific impulse.) There is obviously some limit on flow rate through a given size reactor; this flow rate is dictated by core pressure drop, aerodynamic loads on the fuel elements, or a Mach number limit. The Mach number may be limited by flow distribution sensitivity at high Mach numbers.

Although it is impossible to choose an optimum set of operating conditions from a plot such as this, figure 2 does provide an insight into the requirements for various operating conditions. For example, any effort to increase performance by operation at high values of mass velocity poses three conditions evident in the figure:

- (1) High dynamic head: The fuel elements must be capable of withstanding large aerodynamic forces.
- (2) High pressure drop: The core structure must be capable of supporting large pressure forces. Core pressure drop rapidly reaches excessive values unless high pressure levels are used.
- (3) High inlet pressure: The inlet pressure is the sum of the outlet pressure and the core pressure drop. The significance of high inlet pressure is that the pumping power may exceed the pumping power available from a topping turbine (see ref. 4). Unless special provisions are made to increase the temperature to the topping turbine, additional power would be required from some other turbine involving some sacrifice in specific impulse.

From a fuel-element viewpoint, the dynamic head parameter is of most concern because it may severely limit the performance. The dynamic head that a fuel element can withstand depends on the mechanical properties of the materials and the fuel-element configuration (see section DYNAMIC HEAD LIMITATIONS). The reference-design operating point is indicated by the solid symbol in figure 2 at a mass velocity of 50 lb/(sec)(ft²) (244 kg/(sec)(m²)) and a reactor outlet pressure of 600 psia (44 N/cm²). The corresponding dynamic head is approximately 12 psi (8.27 N/cm²).

Fueled Material Composition

The fueled material proposed for this reactor concept is a cermet of uranium dioxide (UO₂) in tungsten (W). Fabrication of this material, its properties and fuel retention characteristics are discussed in reference 5. The composition of the fueled material (ratio of uranium dioxide to tungsten) involves the consideration of a number of design factors, namely,

- (1) The amount of UO₂ required for criticality
- (2) The effect of fueled material composition on properties
- (3) The fueled material thickness required to withstand aerodynamic forces
- (4) The fuel-element surface area required to achieve a high propellant temperature

The influence of these factors on composition is discussed here in general terms through the development of a few simple equations. The uranium dioxide loading can be written as some fraction λ of the total volume of solid material in the fuel element so that

$$V_{\text{UO}_2} = \lambda(V_{\text{UO}_2} + V_{\text{W}})$$

where V represents the volume occupied by the material identified by the subscript. The total volume of solid can be written in terms of the geometric dimensions. Considering a geometry in which the fueled material has two major surfaces, such as a flat plate, the total volume is given by

$$V_{\text{UO}_2} + V_{\text{W}} = \frac{S}{2} b$$

where S is the total major surface area and b is the fueled material thickness. The definition of equivalent diameter

$$D = \frac{4AL}{S}$$

and the two previous equations can be combined to yield

$$\frac{V_{\text{UO}_2}}{A} = 2 \frac{L}{D} \lambda b \quad (1)$$

The fuel elements must contain sufficient uranium dioxide to

- (1) Satisfy criticality requirements including allowance for excess reactivity to start-up or restart and allowance for fuel which may be lost during operation
- (2) Allow for nonuniform loading to tailor the power distribution

Therefore, a minimum volume of uranium dioxide in a given size core (core size represented by the flow area A in eq. (1)) is established by nuclear considerations to satisfy item (1). Item (2) offers some room for compromise. Also, for any given power distribution, the length to diameter ratio is established by heat transfer. Consequently, the product λb in equation (1) is essentially fixed.

The interplay between λ and b is, therefore, of concern. As λ is decreased, a greater portion of the material is tungsten. The value of b must be increased to keep the product λb constant; this further increases the quantity of tungsten. Tungsten is present only to serve as a structure to hold the fuel. It is desirable to use a minimum quantity of tungsten consistent with this need for two reasons: the reactor will be unnecessarily heavy otherwise, and tungsten is a parasitic absorber of neutrons, even when enriched. The variation in the absorption of neutrons by varying the amount of tungsten was ignored in the constancy of λb .

As λ is increased and b is decreased, the mechanical properties are adversely affected. For example, reference 5 shows the tensile strength at 5000° R (2780° K) to decrease rapidly beyond 30-volume-percent UO_2 . Also, the structure becomes too thin to withstand the aerodynamic forces of the high-velocity hydrogen. The minimum value of b will, of course, depend on the inherent stiffness of the fuel-element configuration.

The selection of values for λ and b , therefore, involves a number of disciplines: nuclear, heat transfer, material properties, and structure. Preliminary studies have shown that a reasonable compromise for this reactor concept is a thickness b of 20 mils (0.508 mm), an average uranium dioxide loading of 20 volume percent, and to allow for variable loading to tailor the power distribution, a maximum uranium dioxide loading of approximately 30 volume percent. Core size and fuel-element configuration may alter this compromise to some extent.

Fuel-Element Configurations

Among the various fuel-element configurations considered were elements made of flat plates, concentric cylinders, tube bundles, and fine grids such as a honeycomb. Fuel-element designs must meet the requirements set by the operating conditions and, in addition, must be of a configuration that can be fabricated. Most of the configurations were of limited interest because of expected performance limitations or fabrication difficulty. Two configurations, however, the concentric cylinder and the honeycomb, were selected for further study and are discussed in the following paragraphs. Both elements are the same size, each has flow passages with an equivalent diameter of approximately 0.125 inch (3.18 mm), and both require variable fuel loading to compensate for self-shielding effects discussed in reference 6. Fabrication of these elements is discussed in reference 5.

Concentric-cylinder configurations. - Early in the program, fueled material was available only in the form of flat plates because of limited tungsten fabrication technology. One of the primary reasons for considering the concentric-cylinder geometry was that this element could possibly be made from plate stock curved to form cylinders of various diameters. The concentric-cylinder configuration is illustrated in figure 3 and is similar to the HTRE (Heat Transfer Reactor Experiment) design of reference 7. Advances in tungsten fabrication technology might permit, at a later date, fabrication of cylinders directly. The cylinder wall thickness would be approximately 20 mils (0.508 mm), and the annular gap between cylinders would be one-half the equivalent diameter or approximately 62 mils (1.59 mm). Each cylinder would have a different uranium dioxide loading per unit volume to achieve uniform radial power within the element. The number of cylinders could vary, and fewer elements would be required in a given size core as the

number of cylinders and, therefore, element diameter is increased. As the fuel elements get larger, however, the self-shielding effects increase, and a greater variation in fuel loading is required. The maximum number of concentric cylinders that can be used without exceeding a uranium dioxide loading of 30 volume percent and still maintain criticality in the reference design is approximately 11 cylinders. This corresponds to a fuel-element diameter of 2 inches (5.08 cm) with the smallest cylinder diameter being 0.5 inch (1.27 cm).

Fuel elements consisting of thin-walled cylinders of this configuration are expected to be dynamic-head limited with the limiting dynamic head dependent on the largest cylinder diameter, the number of support combs, and the cylinder wall thickness. The results of dynamic head tests are discussed in the section Concentric-Cylinder-Element Tests.

Honeycomb configuration. - The honeycomb configuration, illustrated in figure 4, is a rigid structure and may well satisfy the desire for thin-fueled sections without imposing dynamic head as a limiting parameter. The reference-design web thickness is approximately 20 mils (0.508 mm), and the distance across flats of each hexagonal flow passage is approximately 0.125 inch (3.18 mm). The outside diameter of the stage is approximately 2 inches (5.08 cm).

The rigidity of the honeycomb element may pose a thermal stress problem, and experiments conducted to evaluate this problem are discussed in the section Thermal Stress Tests.

Fuel-element arrangement. - The fuel-element assemblies for this reactor concept are proposed to be made of a number of short stages. The full-length fuel-element assembly illustrated in figure 5, would consist of a series of these short stages with each stage individually attached to a support tube. This arrangement is intended to ease fabrication of the elements and also to provide mixing of the hydrogen at various axial locations between stages to minimize hot channels. Each stage in the reference design has an axial length of 1.5 inches (3.81 cm). Further details of the reference fuel-element design are given in reference 3.

Reference-Design Parameter Values

As a result of the interrelation of various parameters, values of these parameters were selected for a reference design. Those reference-design values pertinent to the fuel-element feasibility study are presented as follows:

Reactor outlet propellant temperature, $^{\circ}\text{R}$; $^{\circ}\text{K}$	4500; 2500
Nominal fuel-element temperature, $^{\circ}\text{R}$; $^{\circ}\text{K}$	5000; 2780
Reactor outlet dynamic head, psi; N/cm^2	12; 8.27
Equivalent diameter of flow passage, in.; mm	0.125; 3.18
Fueled material thickness, in.; mm	0.020; 0.508
Average UO_2 in cermet, vol. %	20
Maximum UO_2 in cermet, vol. %	30
Stage length, in.; cm	1.5; 3.81

Further details are given in reference 3.

Two fuel-element configurations, a concentric-cylinder configuration and a honeycomb configuration, were selected for further study. Feasibility investigations of these two geometries about the design point are discussed in the following sections.

DYNAMIC HEAD LIMITATIONS

Fuel elements for the tungsten water-moderated reactor are subject to aerodynamic forces associated with the high-velocity hydrogen flow. These forces are proportional to the dynamic head $\rho v^2/2g$ of the flowing hydrogen.

Experiments conducted on concentric-cylinder fuel elements for nuclear propulsion of aircraft (ref. 8) showed that fuel-element operation is limited by excessive deformation of the fuel cylinders when the operating conditions are too severe. The deformation increased with temperature, time, and stress level, with the limiting combination of these conditions a function of the stiffness of the geometry. Even for short-time operation, where creep is not a factor, a limiting value of dynamic head is to be expected.

A theoretical analysis predicts the limiting or critical dynamic head for plate-type fuel elements (ref. 9). The analysis equates the pressure force necessary to deflect a plate acting as a uniformly loaded beam to the pressure force resulting from velocity changes for the corresponding flow area changes when the plate is deflected. An expression resulted for the critical dynamic head beyond which any small perturbation would lead to failure. The critical dynamic head is expressed in terms of the geometric dimensions and mechanical properties of the fuel-element material. The analysis assumes that the plates are long in the flow direction, and the perturbation leading to failure occurs locally so that it does not alter the flow distribution in parallel channels.

No analytical treatment is available for complex geometries such as the concentric-cylinder element. Furthermore, the elements proposed for the TWMR concept are made

up of a series of stages, each stage relatively short in the flow direction. When the leading edge of the fuel element or fuel-element stage is exposed to the same dynamic head conditions as the downstream sections, the dynamic head is expected to be limited by failure of the leading edge unless the leading edge is reinforced in some manner. Although the analysis of reference 9 cannot be expected to apply directly to leading edge failure, nor to geometries other than plates, the problem remains one of elastic stability and the same basic parameters resulting from the analysis are assumed to be controlling. The critical dynamic head is, therefore, assumed to be a function of (1) a geometry parameter characterizing the geometric form and dimensions and (2) a materials parameter characterizing the pertinent mechanical properties. Because no analytical method was available, the dynamic-head limit for the concentric-cylinder element was determined experimentally.

The critical dynamic head was determined by noting the dynamic head necessary to cause failure during test. Any test of fuel elements at the temperatures of interest (5000°R (2780°K)) poses difficult problems. It requires either high heat-generation rates within the element, or flow through the element of a hot fluid which has been pre-heated to fuel-element operating temperature. The latter approach was used to obtain some data reported herein, but to avoid some of the difficulties associated with high temperature, a method of cold-flow testing was also devised. Because the critical dynamic head of a given geometry fuel element is a function only of the mechanical properties of the material, the proper selection of a room-temperature substitute material for tungsten will provide meaningful data from a test program. Cold-flow tests eliminate the need for high temperatures and for test elements made of tungsten. The latter was especially significant while tungsten fabrication techniques were being developed. Therefore, in order to expedite the test program, a room-temperature material was selected to simulate hot tungsten, and concentric-cylinder elements were constructed of this material. Tests on these elements at room temperature were used to predict the critical dynamic head of their tungsten counterpart at reactor operating temperature. The data were later checked by hot-flow tests on tungsten elements.

Selection of a Substitute Material

Based on the work of reference 9, the mechanical properties pertinent to the dynamic-head limit are elastic modulus and Poisson's ratio, and these appear as a property parameter $E/(1 - \nu^2)$. Poisson's ratio ν does not vary greatly for metals and has a value of approximately 0.3; therefore, it has little influence on the property parameter. Thus, a substitute material is desired that has an elastic modulus at room

~~CONFIDENTIAL~~

temperature equal to that of tungsten at operating temperature. Because of the uncertainty of the high-temperature properties of tungsten and the question of applicability of the information from reference 9 to the case of interest, the selection of material was aided by a series of tests. Flow tests were conducted on a simple fixed geometry (a single flat plate in a flow channel) for various materials at room temperature and for tungsten at high temperature. These tests were designed to determine a material whose critical dynamic head at room temperature was the same as tungsten at 5000° R (2780° K).

Room-temperature flow tests. - Tests were conducted in an air flow facility described in appendix D. The test section shown in figure 6 provided for mounting a single flat plate. Because cold- and hot-flow test results were to be compared, it was important that the geometry, including end supports, was identical. Accordingly, the plate was clamped firmly at one end, but had sufficient clearance at the other end to allow for thermal expansion in the hot-flow tests. All plates tested were 20 mils (0.508 mm) thick with a 2-inch (5.08 cm) span between supports, and an axial length of 2 inches (5.08 cm). The plate for each test was located in the midplane of the duct with a 64-mil (1.62 mm) flow-passage height on each side of the plate. The dimensions were chosen to correspond approximately to proposed fuel-element dimensions of material thickness, axial length, and equivalent diameter.

Tests were conducted on plates of lead, lead - 10 percent antimony, aluminum, and copper. Processing of the plates was carefully controlled to assure uniformity. The plates were rolled to within 1 mil (0.0254 mm) of the specified thickness and sheared to size. The aluminum and copper plates were annealed in a furnace while clamped between flat steel plates to make them flat and uniform in their properties. Each lead plate was flattened by placing it on a flat surface and rubbing it. Since annealing of lead takes place at room temperature, the lead plates became annealed shortly after flattening. Finally, the upstream edge of each plate was deburred but left square.

During each test, the dynamic head was gradually increased by increasing the flow rate until failure occurred. Plate failure was detected by a deflection of the plate sufficient to make contact with a probe on either side of the plate which completed an electric circuit to provide a signal. The probes were located at the leading edge at the mid-span of the plate, and positioned 10 mils (0.254 mm) from the undeflected plate. The 10-mil (0.254 mm) gap was chosen to require a deflection beyond the elastic limit of the materials to be tested. Plate failure signal, therefore, corresponds to permanent deflection of the plate.

The dynamic head at failure was determined from measured values of flow rate, temperature and pressure, and the known flow area at the plates according to

$$\left(\frac{\rho v^2}{2g} \right)_c = \frac{w_c^2 R t}{2g p A^2}$$

~~CONFIDENTIAL~~

The results are shown in figure 7 where the dynamic head at failure is plotted against the elastic modulus of the material. The dynamic head at failure increases with elastic modulus. There is, however, considerable scatter in the data even though precautions were taken to control plate thickness and flatness. Such scatter in the data, if typical for fuel elements, would require a large factor of safety when mean values are used for design.

Hot-flow tests. - Tests of tungsten plates were conducted in a hot-flow facility. The facility included an electric resistance heater to preheat the flowing gas before it entered the test section. A description of the facility is given in appendix E. The test section (fig. 8) provided for a mounting similar to that used for the room-temperature flow tests. The test-section housing material was boron nitride which was chosen because of its refractory nature and electrical insulating qualities. The spacers at the plate supports were made of molybdenum. Electrical contact probes were provided as in the room-temperature flow tests. Although provision for probes at three axial positions was made, only the leading-edge probe was used after initial testing. The end of the plate on one side of the channel was pinned in position. The end on the other side of the channel permitted transverse movement to allow for thermal expansion as the plate was heated. As with the room-temperature flow tests, the plates tested were 20 mils (0.508 mm) thick with a 2-inch (5.08 cm) span between supports and an axial length of 2 inches (5.08 cm). The plate for each test was located in the midplane of the duct with a 60-mil (1.52 mm) flow passage height on each side of the plate.

Hot-flow tests were conducted on tungsten plates using hydrogen as the flowing gas. The plate temperatures were taken to be equal to the stagnation temperature of the flowing hydrogen. The resulting data are shown in figure 9 where the critical dynamic head is plotted as a function of temperature. The curve was extrapolated to zero dynamic head at the melting point of tungsten.

Choice of substitute material. - The primary criterion for a proper room-temperature substitute material was a material with the same critical dynamic head in the flat-plate test as that determined for tungsten at reactor operating temperature.

The proposed fuel-element operating temperature is 5000°R (2780°K). At this temperature the flat plate data for tungsten in figure 9 gives a critical dynamic head of approximately 1 psi (0.7 N/cm^2). Of the materials tested at room temperature, lead or lead - 10 antimony appears to simulate tungsten at operating temperature (fig. 7).

Concentric-Cylinder-Element Tests

Concentric-cylinder fuel-element stages were constructed of lead - 10 antimony material and of tungsten. These were flow tested to determine critical dynamic head.

Lead - 10 antimony material was used to investigate various modifications to the leading edge. Some endurance tests (of the order of hours) were conducted with lead-antimony elements in an effort to determine if creep had any influence on critical dynamic head. Tungsten elements were tested at elevated temperatures, and the results are compared with the lead - 10 antimony results.

Room-temperature flow tests. - Fuel-element stages were fabricated from lead - 10 antimony material for the concentric cylinders. The first series of tests investigated various leading-edge supports. The three different leading-edge supports tested are illustrated in figure 10. All three element types consisted of 11 consecutive cylinders with a center plug. Each cylinder was 1.5 inches (3.81 cm) in axial length and had a wall thickness of 20 mils (0.508 mm). The leading edge of each cylinder was rounded to a radius of one-half the wall thickness. The radial gap between consecutive cylinders was 60 mils (1.52 mm). The first type (fig. 10(a)) had four radial support combs, 90° apart, extending across the radius of the element. These combs were made of brass and were soldered to each of the cylinders at the point of intersection. The second type (fig. 10(b)) had four additional combs supporting the seven outer concentric cylinders, and the third type (fig. 10(c)) had eight additional combs supporting the eight outer concentric cylinders. All the support combs extended into the element an axial distance of 0.12 inch (3.05 mm) beyond the leading edge, and thus, served to support only the leading edge.

The elements were tested individually by placing them in an air duct of the flow facility used for the room-temperature flat-plate tests described in appendix D. The dynamic head was gradually increased by increasing the flow rate until failure occurred. Failure was detected by an increase in pressure drop across the element and by observing the element in the optical system described in appendix D. Five elements were tested: two elements with four radial support combs, two elements with eight radial support combs, and one element with 12 combs. The critical dynamic heads for these elements are tabulated as follows:

Number of radial support combs	Critical dynamic head, psi; N/cm ²	Figure
4	14.4; 9.93	10(a)
4	11.0; 7.58	10(a)
8	25.6; 17.6	10(b)
8	26.8; 18.5	10(b)
12	29.8; 20.5	10(c)

The data indicate an appreciable increase in dynamic head capability as the number of radial support combs is increased from four to eight. This improvement is attributed to the decrease in span as more supports are added. Motion pictures (using the optical

system described in appendix D) taken during the tests indicate that failure of these two types of elements starts at the leading edge. A typical failure is shown in figure 11. A Lewis motion picture C-240, available on loan to qualified requesters, presents several sequences of failures of concentric-cylinder elements. A request card and a description of the film are included at the back of this report.

Increasing the number of radial supports from 8 to 12 offers little improvement. Examination of individual motion-picture frames shows that failure of the element with 12 radial support combs started at the downstream end. Thus, the addition of further supports at the leading edge cannot be expected to increase the critical dynamic head.

The effect of creep on critical dynamic head was studied by testing three additional elements with four radial support combs for extended periods. The first element was run at a dynamic head of 12.6 psi (8.69 N/cm^2) for 1.2 hours after which the dynamic head was decreased to 10.2 psi (7.04 N/cm^2) for 1.3 hours when it failed. The second element was run at a dynamic head of 12.6 psi (8.69 N/cm^2) for 0.9 hour after which the dynamic head was decreased to 11.3 psi (7.80 N/cm^2) for 1.6 hours when the element failed. Both elements demonstrated the capability of operating at a dynamic head of 12.6 psi (8.69 N/cm^2) but failed at less severe conditions after some period of operation. The third element failed after 32 hours of operation at a dynamic head of 8 psi (5.52 N/cm^2). Failure at a dynamic head less than the critical short-time value for all three elements indicates that creep under load is a factor which must be considered.

The observation of failure starting at the leading edge suggested that approaches other than additional supports might improve the dynamic-head capability of these elements. Scalloping the leading edge between supports was considered as a means of stabilizing these edges. Therefore, tests were run on two elements of the type shown in figure 12. The elements were identical to the elements of figure 10(a) except for the leading-edge contour. The elements failed at dynamic heads of 18.9 and 21.7 psi (13.0 and 15.0 N/cm^2) compared with 11.0 and 14.4 psi (7.58 and 9.93 N/cm^2) for the elements with a plane leading edge.

Hot-flow tests. - Although the lead-antimony tests predicted the capability of tungsten elements reasonably well, some check points on hot tungsten elements were deemed necessary. The hot-flow facility used for single plates of tungsten did not have the flow-rate capacity required for full-scale testing of concentric-cylinder tungsten elements. An arc-jet facility at the NASA Langley Research Center was used for the tests. For the tests described herein, the desired temperatures were achieved by allowing some of the gas to bypass the arc and mix with the heated gas before entering the test section. This necessitated a redesign of the electrodes. With the exception of this modification, the facility was the same as that described in reference 10. A water-cooled copper nozzle was constructed to house the test elements. An extension was added to provide a flow area downstream of the test section less than the flow area of the test element. This

was done to preclude choking of the flow in the test section and to prevent atmospheric air from coming into contact with the element during test. Nitrogen was used as the flowing gas. Flow-rate limitations and restriction to subsonic flow in the test element limited the maximum dynamic head to 12 psi (8.27 N/cm²). The gas temperature was determined from the measured flow rate and pressure at Mach 1 existing at the known flow area of the nozzle extension. The test temperature measurement was supported by post-test inspection of iridium and molybdenum wires attached to the test elements.

Of the six tungsten elements tested, the first three were inadvertently subjected to temperatures well above that desired and failed at an unknown dynamic head. Of the next three elements tested, two elements had four radial support combs at the leading edge, (figs. 13(a) and (d)) and one element had eight radial support combs at the leading edge (figs. 13(b) or (c)). The temperature monitor wires are visible in the figure. The tungsten elements differed from the lead-antimony elements in that the cylinders of the tungsten elements were supported from the support tube by two 3/16-inch diameter (4.76 mm) pins passing through holes in the cylinders. The pins were at 90° to each other and extended across the diameter of the element into the tungsten support tube. The pins were located so that their centers were 0.3 and 0.5 inch (7.62 and 12.7 mm) downstream of the leading edge. Because failure of the lead-antimony elements of these types started at the leading edge, the pins were not considered to influence the dynamic head capability. The test conditions and results for the three elements are summarized in the following table:

Number of radial support combs	Temperature, °R; °K	Dynamic head, psi; N/cm ²	Remarks
4	5150; 2860	11.5; 7.93	No failure
4	5530; 3070	12.0; 8.27	Failure
8	5400; 3000	12.0; 8.27	No failure

As indicated in the table, an element with four radial support combs was tested at a temperature of 5150° R (2860° K) and a dynamic head of 11.5 psi (7.93 N/cm²) without failure. Inspection of the temperature monitor wires showed the iridium wire (melting point 4910° R (2730° K) to be melted, but the molybdenum wire (melting point 5210° R (2890° K) had not melted. Because of the facility limitations, the dynamic head could not be increased to failure. The temperature for the next element was increased, and the element failed during a transient from 5150° to 5530° R (2860° to 3070° K) at a dynamic head of 12 psi (8.27 N/cm²). The last element, with eight radial support combs, was tested at a temperature of 5400° R (3000° K) and a dynamic head of 12 psi (8.27 N/cm²), but the element did not fail. In the latter two tests, both the iridium and molyb-

denum wires had melted. No duration testing of the tungsten elements was done because of the limited electrode life and gas supply available at the facility.

Dynamic-Head Limitations

The dynamic-head capability of concentric-cylinder fuel elements has been determined from experiments on lead-antimony elements at room temperature and tungsten elements at elevated temperatures. An alloy of 90-percent lead - 10-percent antimony was selected as a room-temperature material to simulate tungsten at 5000°R (2780°K) on the basis of available property comparisons and flow tests on single flat plates of each material.

The dynamic-head capability of concentric-cylinder elements was shown to improve considerably, as expected, by increasing the number of supports at the leading edge. For example, the critical dynamic head of a 2-inch-diameter (5.08 cm) element was increased from approximately 12 psi (8.27 N/cm^2) with four radial supports to 26 psi (17.9 N/cm^2) with eight radial supports. Contouring the leading edges by scalloping the leading edge between supports also offers some improvement in dynamic-head capability. The critical dynamic head decreased with operating time indicating that creep may significantly influence the limiting dynamic head.

Although data were obtained on only three tungsten elements at elevated temperature, the available data indicate that the lead-antimony alloy simulates tungsten at a temperature somewhat higher than 5000°R (2780°K).

The data show that the concentric-cylinder configuration may be suitable for the reference-design dynamic head of 12.5 psi (8.62 N/cm^2). However, the limited number of specimens tested and the noticeable effect of creep during operation leave unanswered questions with regard to the feasibility of the concentric-cylinder design. If many more than eight radial supports were required, this configuration would start to approach the honeycomb. In any case, there is a limit on the dynamic-head capability of the concentric-cylinder design. While this limit may be compatible with the reference design, it may be the first limit reached in a reactor designed for higher performance.

THERMAL STRESSES IN HONEYCOMB FUEL ELEMENT

The rigidity of a fine-geometry fuel element such as a honeycomb eliminates the problem of aerodynamic stability. This inherent stiffness may, however, inhibit relative expansion to the point where thermal stresses become excessive. These

thermal stresses are dependent on the temperature distribution within the element and on the properties of the material.

Temperature distribution is dependent upon fuel distribution, neutron flux distribution, variation in coolant flow rate, dimensional variations, and thermal conductivity of the fuel-element material. Because of the many factors which must be carefully controlled, it is virtually impossible to achieve uniform temperature within a fuel element. By careful analysis and control of tolerances, the temperature gradients can be minimized but not eliminated. The problem therefore becomes one of designing a fuel element that will withstand stresses associated with the remaining temperature gradients.

The honeycomb was considered capable of withstanding thermal stresses introduced during operation without difficulty, and the combination of high strength and ductility of tungsten at high temperature should be adequate for any reasonable reactor situation. Plastic flow at high temperature would essentially preclude high stresses. The end result of such plastic flow or inelastic strains, however, was of concern. The problem could occur as follows: Thermal stresses would cause inelastic strain at temperature (1) by plastic flow as stresses are applied and (2) by creep under these stresses during reactor operation. Because these strains are inelastic, low-temperature stresses would appear as the honeycomb cools and tries to return to its original unstrained condition. At room temperature, tungsten is strong but brittle, and the internal stresses might cause the honeycomb to crack. The situation is aggravated by thermal cycling where thermal fatigue may occur. It is difficult to determine how the honeycomb deforms in this inelastic manner. Thus, no estimates could be made of the low-temperature stresses nor were any data available on the ability of the material to withstand thermal fatigue.

In order to evaluate the thermal-stress problem, temperature gradients which might be expected were calculated and similar temperature gradients were imposed experimentally on a uniformly loaded honeycomb stage at high temperature. The element was thermally cycled under thermal stress conditions and subsequently examined for evidence of failure.

Temperature Distribution

The thermal stresses in the honeycomb fuel element depend primarily on the temperature distribution within the element. Although the nominal design may be for uniform temperature in each of the fuel-element stages of the reactor, lack of detailed knowledge and inability to control many design parameters will result in nonuniform temperature or hot spots.

The desired uniform temperature in a honeycomb stage could be achieved with uniform power distribution with the assumption that all the flow passages are of equal size, the coolant inlet temperature is uniform, and there is no radial heat loss. Honeycomb fabrication studies have indicated that passage size can be controlled within 1 mil (0.0254 mm) of the nominal value. Therefore, if extensive mixing of the coolant occurs in the spaces provided between stages, the main factor influencing the temperature profile within a stage is the power distribution.

Power distribution within a stage is dependent on the neutron flux distribution and the distribution of fuel within the stage. Neutron flux is calculated taking into account the self-shielding effects of the fuel. A decreasing flux and a changing of the flux spectrum toward the center of the element results. A radial variation in fuel loading is then prescribed to compensate for these effects in order to approach uniform radial power. These radial variations within the element were considered to be the most difficult to predict and control. Therefore, temperature variations in the radial direction were investigated.

In addition to the radial distribution of temperature, local temperature gradients were also studied. While small step changes in fuel loading may occur locally, the mean path length of the neutrons is finite and thus precludes discontinuities in the flux distribution. Consequently, rapid local changes in power (e. g., from web to web in the honeycomb) can occur only as a result of local fuel loading variations. The temperature variations which could occur in adjacent webs were studied on this basis.

Local temperature gradients. - Local temperature gradients can occur as a result of step changes in fuel loading. Obviously the temperature difference which results is dependent on the size of the region in which the step change occurs and on the magnitude of change. Because the fuel is dispersed in the tungsten as discrete particles of uranium dioxide, a microscopic view would show regions of zero fuel and regions of total fuel. Even though the step changes in this case are large, the regions involved are so small that the temperature differences must be extremely small. What is of more concern is the local variation which might occur on a macroscopic scale such as from one web to another in the honeycomb. The change in fuel loading in this situation is limited to the minimum tolerances inherent in the honeycomb fabrication process.

Consider the case where one web in a honeycomb has a heat-generation rate which differs by a factor K from the rest of the honeycomb. Because of the difference in heat-generation rates, this web will run at a higher or lower temperature than the rest of the honeycomb depending on whether K is greater or less than 1. Thus, if K is greater than 1, some of the heat generated in the web is transferred to the propellant, and some of the heat is transferred by conduction through the webs to the rest of the honeycomb. It is desired to determine, for a given value of K , the amount of overtemperature when thermal conduction effects are included.

A model of this heat-flow problem is illustrated in figure 14. Because of symmetry, only one-fourth of the web in question needs to be considered. The model is conservative in that the heat flow path from this quarter web was taken to be one web extending to infinity. Actually, the honeycomb geometry is such that the heat-flow path increases in area by additional webs which would act as cooling fins.

This model can be reduced to a one-dimensional problem if the webs are thin and the triangular section, where the webs meet, is small and can be neglected. Then, the following equation applies:

$$\frac{d^2 T}{ds^2} + \frac{q''' }{k_w} = \frac{2h}{k_w b} (T - T_b) \quad (2)$$

This equation can be made nondimensional by the following definitions:

$$\theta = \frac{2h(T - T_b)}{q''' b}$$

$$Q^2 = \frac{2hu^2}{k_w b}$$

and

$$\eta = \frac{s}{u}$$

Substitution of these identities into equation (2) yields

Heat-generation rate, Kq''' :

$$\frac{d^2 \theta}{d\eta^2} = Q^2(\theta - K) \quad \text{for } 0 \leq \eta \leq 1$$

Heat-generation rate, q''' :

$$\frac{d^2 \theta}{d\eta^2} = Q^2(\theta - 1) \quad \text{for } 1 \leq \eta < \infty$$

The general solution for each zone is

$$\theta = K + C_1 e^{Q\eta} + C_2 e^{-Q\eta} \quad \text{for } 0 \leq \eta \leq 1$$

$$\theta = 1 + C_3 e^{Q\eta} + C_4 e^{-Q\eta} \quad \text{for } 1 \leq \eta < \infty$$

The constants C_1 , C_2 , C_3 , and C_4 were determined from the following boundary conditions:

at $\eta = 0$, $dT/d\eta = 0$

at $\eta = \infty$, $dT/d\eta = 0$

at $\eta = 1$, temperature and heat continuity exist

The equation for the maximum temperature difference for the preceding boundary conditions is

$$\frac{T_0 - T_\infty}{T_\infty - T_b} = \frac{(K - 1)(3e^Q + e^{-Q} - 4)}{(3e^Q + e^{-Q})}$$

where $T = T_0$ at $\eta = 0$, and $T = T_\infty$ at $\eta = \infty$.

The maximum temperature difference in the example $T_0 - T_\infty$ is therefore a function of K , Q , and $T_\infty - T_b$. Using the expression for heat flux $q_\infty'' = h(T_\infty - T_b)$ gives the nondimensional parameter Q as

$$Q = \sqrt{\frac{q_\infty'' 2u^2}{(T_\infty - T_b)k_w b}}$$

For the conditions of interest, fixed values of μ , b , k_w , and K were chosen for the honeycomb, and the maximum temperature difference in the honeycomb is plotted in figure 15 as a function of $(T_\infty - T_b)$ for several values of the heat flux q_∞'' . The values chosen were

One-half width of web, u , in.; mm	0.0361; 0.917
Fueled material thickness, b , in.; mm	0.020; 0.508
Web thermal conductivity, k_w , Btu/(sec)(in.)(°R); J/(sec)(cm)(°K)	9.28×10^{-4} ; 0.694
Ratio of heat-generation rates, K	1.1

The heat flux will vary throughout the reactor core depending on the compromise reached on heat-removal capability and the ability to tailor the power distribution. The axial variation in heat flux for the reference design can be expressed in terms of the surface and bulk fluid temperatures both of which vary axially. This variation in q''' as a function of $T_\infty - T_b$ was obtained from reference 3 and is shown in figure 15 as a dashed line. This line represents the highest power fuel-element assembly in the reference reactor and is therefore the most severe case for the reference design.

As shown in figure 15, the maximum temperature difference in the honeycomb webs for the reference design is 80°R (44°K). The stresses resulting from this situation in a complex honeycomb geometry are difficult to evaluate rigorously. However, an estimate can be made on a conservative basis as follows: Consider the entire web in question to be operating at its maximum temperature T_0 and the rest of the honeycomb to be operating at its minimum temperature T_∞ . Then, if the high-temperature web were to be fully restrained by the surrounding honeycomb structure, the stress in the web would be

$$\sigma = E\alpha(T_0 - T_\infty)$$

Obtaining values of E and α from reference 5 for 30-volume-percent UO_2 in tungsten at 5000°R (2780°K) to be

Young's modulus of elasticity, E , psi; N/cm^2 12×10^6 ; 8.27×10^6
 Linear coefficient of expansion, α , $(^\circ\text{R})^{-1}$; $(^\circ\text{K})^{-1}$ 4.48×10^{-6} ; 7.90

and a maximum temperature difference from figure 15 equal to 80°R (44°K) gives the resulting stress of 4320 psi (2920 N/cm^2). This value is approximately equal to the ultimate tensile strength of the material given in reference 5. Because of the conservative nature of the calculations based on elastic behavior, the material will not fail under these conditions, and the stress will decrease as the material is subject to creep. Such plastic flow will cause stress when the entire honeycomb is cooled to a uniform temperature and may present a problem if thermally cycled. In order to estimate the magnitude of this problem, one can consider creep at operating temperature to the extent that the stress is reduced to zero. This condition represents maximum plastic flow and a maximum strain at uniform ambient temperature. Again, if all the strain takes place in the web in question, the unit strain is given by

$$\epsilon = \alpha \Delta T$$

$$= 4.26 \times 10^{-6} \times 80 = 348 \times 10^{-6} \text{ in./in. or cm/cm}$$

The resulting stress at room temperature is therefore

$$\sigma = \epsilon E$$

Using a value of E of 50×10^6 psi (34.5×10^6 N/cm²) from reference 11 for tungsten at room temperature, the room-temperature stress is 17 400 psi (12 000 N/cm²), which is 25 to 30 percent of the yield strength of recrystallized tungsten given in reference 11 (no data are available for the room-temperature elastic limit of W-UO₂ cermet). The material can therefore be expected to accommodate this strain elastically, and no adverse effect of thermal cycling is anticipated. Therefore, the thermal stress in the honeycomb resulting from local 10-percent step changes in power ($K = 1.1$) are not expected to cause failure at the reference design conditions. At power densities greater than the reference-design conditions, this situation may require reexamination.

Radial temperature profile. - Difficulties in predicting the desired radial fuel loading variations and in achieving these prescribed variations during fabrication are the primary cause of nonuniform power distribution. Radial temperature variations will therefore, be present.

Fabrication tolerances will allow uncontrolled variations in fuel loading within certain limits. For example, web thickness will vary from the prescribed nominal value of 0.020 inch (0.508 mm). Also, the actual fuel volume percent in the web will deviate from the prescribed amount. Fabrication methods developed during the course of this program experienced difficulties in controlling web thickness better than 0.020 ± 0.001 inch (0.508 ± 0.025 mm) and UO₂ content better than 20 ± 1 volume percent. The degree to which these parameters can be controlled in production with further development is not known. It was assumed that the combined effect of inaccuracies and tolerances would allow a 10-percent variation (± 5 percent) in power generation. Although the deviations may be random and occur in small local regions and thus produce only small effects, it is also possible that they occur in large radial regions. The effect of deviations occurring over large radial regions was determined by calculating temperature profiles with various radial regions differing in heat-generation rate by 10 percent from the rest of the element.

A honeycomb fuel element is a fine-geometry structure and, for the purpose of the calculations, was considered as a homogeneous porous body. Heat is generated within the structure, transferred from the hot metal surface to the cooling gas, and conducted to adjacent areas.

Consider a cylindrical body with constant heat-generation rate q''' , constant thermal conductivity k , and a constant heat-transfer coefficient h . The differential equation from a heat balance is

$$\frac{d^2T}{dr^2} + \frac{1}{r} \frac{dT}{dr} + \frac{q'''}{k} - \frac{h}{k} B(T - T_b) = 0 \quad (3)$$

where B is the heat-transfer surface area per unit volume.

The heat-generation rate q''' within a radial region of the honeycomb will be considered constant. The heat convected to the cooling gas varies with metal temperature. The difference between the two terms

$$q'''_{\text{net}} = q''' - hB(T - T_b)$$

then represents the local heat input which must be transferred by conduction. This net internal heat generation varies linearly with metal temperature. The case of radial heat conduction in a solid circular cylinder with internal heat generation that varies linearly with temperature was investigated by Jakob in reference 12. With proper identification of terms, the differential equation presented by Jakob is identical to equation (3).

Defining $n = hB/k$ and applying a transformation where

$$N = \frac{q'''}{k} + n(T_b - T)$$

give equation (3) in the familiar form of a Bessel zero-order differential equation:

$$\frac{r^2 d^2 N}{dr^2} + \frac{rdN}{dr} - nr^2 N = 0$$

The general solution is

$$N = C_1 I_0(r\sqrt{n}) + C_2 K_0(r\sqrt{n}) \quad (4)$$

where $I_0(r\sqrt{n})$ and $K_0(r\sqrt{n})$ are the symbols for the modified Bessel function of zero order and of first and second kind. The constants of integration C_1 and C_2 are determined from boundary conditions. Equation (4) was used to calculate radial temperature profiles. The heat-generation rate q''' is a constant within a given region and any change has to be applied as a step change. These constants, C_1 and C_2 , must be evaluated from each of the radial areas where the heat-generation rate is changed. When the area including $r = 0$ is calculated, C_2 must equal zero in order that $dT/dr = 0$ at $r = 0$.

The conditions existing at the first stage of the reference-design reactor were chosen to demonstrate the effect of a change in heat-generation rate on the temperature and stress profiles. At this point in the reactor, a surface temperature of 3130°R (1740°K), a coolant temperature of 500°R (278°K), and a heat-transfer coefficient of $2.01 \times 10^{-3} \text{ Btu}/(\text{sec})(\text{in.}^2)(^{\circ}\text{R})$ or $0.594 \text{ J}/(\text{sec})(\text{cm}^2)(^{\circ}\text{K})$ were obtained from information given in reference 3.

The effective thermal conductivity k of a honeycomb model was evaluated from measurements made on models cut from electrical conducting paper. The radial electrical resistance for a honeycomb pattern was compared with a solid (no holes) pattern. For the geometry of interest, the ratio of resistance for a honeycomb to a solid was 6.7. An effective thermal conductivity for the model of $1.40 \times 10^{-4} \text{ (Btu}/(\text{sec})(\text{in.})(^{\circ}\text{R})$ or $0.1048 \text{ J}/(\text{sec})(\text{cm})(^{\circ}\text{K})$ was used.

The boundary conditions existing on the outer radius of the fuel-element model also had to be defined. The effect of nonuniform flow passages at the periphery of the honeycomb resulting from the cylindrical geometry is treated in reference 3. It was assumed here that the passages are uniform to the outer radius of the model and that an annular space of 0.010 inch (0.254 mm) exists between the cylindrical model and the support tube. The radiative heat-transfer area was taken to be the area of the outer cylindrical surface. The effective convection heat-transfer area represents the ends of the webs that are exposed by cutting the honeycomb into a cylinder and was taken to be 15 percent of the outer cylindrical surface. If the support tube is assumed to be at the gas temperature, a combined convection and radiation heat-transfer coefficient based on the total cylindrical surface area may be defined as

$$h'_p 0.15 S(T_s - T_b) = h_p 0.15 S(T_s - T_b) + CS(T_s^4 - T_b^4)$$

The radial heat flux at the outer surface of the model is therefore given by

$$q'' = 0.15 h'_p (T_s - T_b)$$

The convective heat-transfer coefficient at the periphery h_p was related to the heat-transfer coefficient in the honeycomb by assuming a mass velocity in the annulus that would produce the same friction pressure drop in the annulus as in the hexagonal passages of the honeycomb. This value of h_p was then augmented by the radiation term to give a value for h'_p of $1.15 \times 10^{-3} \text{ Btu}/(\text{sec})(\text{in.}^2)(^{\circ}\text{R})$ or $0.339 \text{ J}/(\text{sec})(\text{cm}^2)(^{\circ}\text{K})$.

The radial temperature profiles for various heat-generation distributions were calculated from equation (4) by using the conditions previously stated. Figure 16 shows eight heat-generation distributions and the corresponding temperature profiles. Line A

of figure 16(b) is for uniform heat-generation rate, as shown in figure 16(a). Because of radial heat loss, the temperature decreases in the outer region, as shown by line A in figure 16(b). In order to achieve a uniform temperature profile, the heat-generation rate would have to increase exponentially near the outer radius. This variation in heat-generation rate is not practical because it would require an infinite heat-generation rate at the outer surface. A practical approach to uniform temperature can be achieved by increasing the heat generation in the outer 0.070 inch (1.78 mm) by 6 percent, as indicated by line B in figures 16(a) and (b). These curves were used to represent a design radial temperature profile in the first stage of the reactor which could be achieved in practice by increasing the UO_2 content or by increasing the web thickness in the outer region.

Changing the heat-generation rate within certain radial zones alters the temperature profile and induces thermal stress. A 10-percent variation in power generation due to tolerances may be expected. A 10-percent change from line B was applied to various radial regions. A 10-percent change in heat-generation rate was applied to the outer 0.145 inch (3.68 mm) (1 hexagonal dimension) to calculate the temperature profiles C and D. Curve C represents a +10 percent change, and curve D represents a -10 percent change. For both cases, the maximum temperature variation from the centerline temperature of 3130°R (1740°K) is about 250°R (139°K). For case D, the outer 0.145 inch (3.68 mm) has a temperature difference of about 150°R (83°K).

Lines E to H represent the temperature profiles for a 10-percent variation in heat-generation rate over larger radial areas. When case G is compared with case H, case G indicates the change in the temperature profile due to a change in heat-generation rate in a small central area. The slope of the curves at the outer radius is controlled by the amount of heat transferred radially through the outer surface. If the heat loss is greater or less than that specified here, the slope will change directly.

The thermal stress parameter $\sigma(1 - \nu)/\alpha E$ for radial, tangential, and axial stresses was calculated by using the temperature profiles shown in figure 16 and equations for a cylinder based on elastic theory from reference 13. This parameter is plotted as a function of radius in figure 17. The curves indicate the stress prior to plastic flow or creep. Figure 17 shows that the greatest tensile stress comes about when the outer 0.145 inch (3.68 mm) is at the reduced heat-generation rate, line D. The greatest compressive stress occurs when a positive change in heat generation occurs in a small central portion of the fuel element, line G.

It should be emphasized that the equations used to develop figure 17 were based on elastic theory. Also, it was assumed that the cylinder was an isotropic material. A honeycomb is obviously not isotropic; a web structure exists in the radial direction, and a column-type structure exists in the axial direction. The effect of the differential expansion of UO_2 and tungsten should also be considered in evaluating the stresses.

Despite these qualifications, the calculated values are indicative of the relative stresses for the cases investigated. Calculation of elastic stress from the stress parameter results in local stress beyond the ultimate strength. The actual stresses would be greatly reduced because of inelastic behavior. In order to determine if thermal stress is a serious problem in the honeycomb, testing is required, and these tests must include thermal cycling because of the possibility of thermal fatigue.

Thermal Stress Tests

The variation of honeycomb-fuel-element radial-temperature profiles with power distribution was presented in the preceding section. Stresses resulting from profiles such as these cause plastic flow and creep to occur at temperature. On cooling down, low-temperature stresses result within the honeycomb. The experimental determination of the ability of a honeycomb to withstand these stresses is the subject of this discussion.

Temperature gradients were imposed on honeycombs by flowing hot hydrogen through a central portion of the honeycomb while cooling the outer periphery with flowing nitrogen, as shown in figure 18. A honeycomb is sandwiched between two molybdenum disks. The disks are relieved on the surfaces facing the honeycomb to minimize contact area, thereby reducing axial conduction losses from the honeycomb. The shape of the disks can be seen in the cutaway drawing of figure 18. The honeycomb and disks are centered within a cylindrical molybdenum container and held in place by a flange bolted to the container at the top and the lip of the container at the bottom. This assembly is placed inside a water-jacketed housing which is located above a gas heater.

Hot hydrogen is then forced to flow through the 19-hole central region of the honeycomb. The periphery of the honeycomb is cooled by nitrogen flowing circumferentially in the annulus formed by the outside of the honeycomb and the inside of the molybdenum container. Four inlets, 90° apart, supply the cold nitrogen and four outlets located symmetrically between the inlets exhaust the nitrogen. A zone without flow exists between the heated and cooled regions. The temperature gradient in this zone and hence the thermal stresses may be varied by increasing or decreasing the nitrogen flow rate. Twelve thermocouples were placed in this no-flow zone to measure the radial temperature gradient. These thermocouples were located at two radial positions with six thermocouples at each position evenly spaced circumferentially and centered axially within the honeycomb passages.

The best available honeycombs consistent with the present state of the art were fabricated and tested. The honeycombs were produced by hot isostatic compaction, discussed in reference 14, using tungsten-coated UO_2 particles.

A thermal cycling test was performed on a honeycomb containing 20-volume-percent UO_2 stabilized with 10-mole-percent calcium oxide under the following conditions:

Number of 10-min cycles	25
Hot gas temperature, $^{\circ}\text{R}$; $^{\circ}\text{K}$	4500; 2500
Temperature gradient in no-flow zone per hexagon, $^{\circ}\text{R}$; $^{\circ}\text{K}$	150; 83
Nominal heating and cooling rates, $^{\circ}\text{R}/\text{sec}$; $^{\circ}\text{K}/\text{sec}$	30; 16

The number of thermal cycles (25) corresponds to the restart requirement goal including restarts for development testing. The hot gas temperature was limited to 4500°R (2500°K) because of the limitations of calcium oxide as a stabilizing agent at higher temperatures (see ref. 5). The temperature of the honeycomb in the heated zone was estimated to be within 200°R (111°K) of the gas temperature. The temperature gradient of 150°R (83°K) across a hexagonal flow passage was chosen on the basis of the analysis in the preceding section. No full temperature profile is presented. A method of calculating the profile is discussed in appendix F. The heating and cooling rates chosen are considered to be reasonable values for reactor startup and shutdown. However, midway through the test, a rapid shutdown occurred because of a heating element failure that resulted in a honeycomb cooling rate in excess of 1000°R per second ($556^{\circ}\text{K}/\text{sec}$).

Inspection of the honeycomb before and after testing both by comparison of photographs and eddy current probing showed no effects on the honeycomb fuel-element stage as a result of the stresses imposed. Nondestructive inspection using eddy current probes is discussed in reference 15. The thermally cycled honeycomb then was cut into two equal cylinders, and one-half was mounted and polished. Inspection of the microstructure confirmed the integrity of the honeycomb throughout. No cracks were evident from this inspection, as illustrated in the photomicrograph of figure 19 taken after testing, which was typical of the entire honeycomb.

The remaining half of this honeycomb was then subjected to a more severe test for a single cycle with a hot gas temperature of 4950°R (2750°K) for 10 minutes. The thermal gradient was 450°R (250°K) across a hexagonal passage. Inspection of the honeycomb by the same methods indicated that there was not failure within the honeycomb structure due to these more severe conditions.

A second honeycomb containing 33-volume-percent UO_2 stabilized with 10-mole-percent yttrium oxide was also tested. The fuel loading for this honeycomb was approximately equal to the maximum fuel loading for the reference design. The honeycomb was cycled three times at temperature gradients of 265, 305, and 465°R (147 , 170 , and 258°K) per hexagonal passage. The hot-gas-zone temperature was maintained at 4900°R (2780°K). The honeycomb was polished and inspected both under a microscope and by the eddy-current technique. Again no structural change was observed.

Thermal Stress Results

Thermal stresses are likely to be present in a fuel element because it is virtually impossible to control the many design parameters necessary to achieve uniform temperature. Uncontrolled variations in power density were estimated to be ± 5 percent. The inherent stiffness of a honeycomb element inhibits relative expansion. Therefore, thermal stresses in a honeycomb were investigated.

Calculations of stresses for estimated maximum local variations in power density of 10 percent indicate no adverse effects on the honeycomb. A study of 10-percent radial variations in power density result in temperature differences across one hexagonal passage of approximately 150 R° (83 K°) for the reference design. Of those cases studied, the most severe thermal stresses occurred when an outer region of the honeycomb had a heat-generation rate 10 percent lower than the rest of the honeycomb.

Experiment showed that thermal stress from a temperature gradient similar to that which can be anticipated during reactor operation at reference-design conditions is not a serious problem. A honeycomb with 20-volume-percent UO_2 withstood 25 thermal cycles with a radial temperature gradient of 150 R° (83 K°) per hexagonal passage. Half of this honeycomb was tested with hot gas at 4950° R (2750° K) and with a temperature gradient of 450 R° (250 K°) per hexagonal passage. The honeycomb showed no sign of failure. A second honeycomb containing a uniform fuel loading of 33 volume percent of UO_2 withstood three thermal cycles with temperature gradients varying from 260 R° (144 K°) to 400 R° (222 K°) per hexagonal passage.

SUPPORT STRUCTURES

The support of the fuel element is an important consideration in the design of the reactor core. To understand the requirements of a fuel-element support structure better, a brief description is required. Figure 5 illustrates the important components associated with the proposed fuel-element arrangement.

In this arrangement, the fuel-element stages are attached individually to a tungsten support tube, which for the reference design has an overall axial length of 55 inches (140 cm). This attachment must withstand the axial drag loads resulting from the hydrogen propellant passing through the passages of the individual fuel-element stages. Also, this attachment must be able to accommodate any relative thermal expansion between the fuel-element stage and the support tube.

The tungsten support tube holding the individual fuel-element stages is fastened at the cold inlet end of the reactor. The combination of brittle materials and long support-tube length requires a lateral support to reduce the bending stresses and to center the

support tube within the aluminum pressure tube. The fuel-element stages and support tube are subjected to lateral loads resulting from ground handling, chemical rocket boost, and in-flight maneuvers. The lateral support must transfer part of these loads from the support tube to the colder aluminum pressure tube. In addition, the lateral support must accommodate relative expansion between the two tubes. These functions must be accomplished without providing a heat conduction path that will overheat the aluminum tube at the points of contact.

Axial support experiments were conducted to evaluate two methods of attachment between the individual fuel-element stages and the support tube. These methods of attachment were evaluated at operating temperature by using simulated drag loads.

Lateral support experiments were conducted to evaluate a proposed lateral support design. Tests were run at operating temperature in a furnace to evaluate the thermal expansion behavior. Room-temperature vibration tests were conducted covering a frequency range of 5 to 2000 cps (5 to 2000 Hz). Static load-deflection measurements were also made.

Axial Support Tests

Tests were conducted to evaluate the attachment between the fuel element stage and the support tube. The primary attachment requirement is to support each fuel-element stage under the axial aerodynamic drag loads for the operational goal of 10 hours at temperature.

The desired operating temperature is 4000°R (2220°K) which is the maximum support temperature expected in the last stage of the reference design (see ref. 3). The maximum calculated drag load on the last stage of the reference design is 20 pounds (89 N) corresponding to a dynamic head of 12.5 pounds per square inch (8.6 N/cm^2).

The combination of axial drag load and temperature conditions were mocked up in a vacuum induction furnace. Figure 20 illustrates the test arrangement. The induction coil was located around the support tube that served as a susceptor and was thus heated inductively. Radiation and conduction between the support tube and honeycomb resulted in a uniform temperature throughout the test assembly after steady state was reached. Consequently, the relative expansion between the support tube and the fuel stage was only due to expansion of dissimilar materials (fueled and unfueled tungsten) at the same temperature.

Two distinct methods of attachment between the fuel stage and the support tube were tested: a metallurgical attachment and a mechanical attachment. Although a honeycomb stage was used for these tests, the basic attachment technique could be ap-

plied to other fuel-stage designs. The honeycomb stages used in the tests contained 20-volume-percent unstabilized UO_2 .

Weights simulating aerodynamic drag loads were applied to a triangular plate positioned on three blocks resting on a honeycomb stage. The load applied to the honeycomb was transmitted through the attachment to the support tube. Care was exercised to ensure uniform loading of the attachment.

Attachment temperature was measured with an optical pyrometer. The pyrometer was sighted into holes in tungsten pins which were inserted into honeycomb passages adjacent to the attachment area. The depth to diameter ratio of the holes in the pins was sufficient to achieve blackbody conditions.

The test program goal of 10 hours of operation at temperature consisted of five 2-hour cycles at 4000°R (2220°K) with an additional 15 minutes to each cycle for heating and 15 minutes for cooling. After each 2 hours at temperature, the furnace was shut down, and the attachment was inspected. Some thermal cycling was thereby imposed by the nature of the test procedure.

Mechanical attachment evaluation. - The mechanical attachment consisted of six pins fitted through close-tolerance holes shown in figure 21. The holes were located in both the reinforced support tube and in tabs bonded to the honeycomb fuel-element stage, as illustrated in figure 22.

An axial load of 25 pounds (111 N) was applied to this attachment which is a 25 percent increase above the calculated reference-design load on the last fuel-element stage. Dimensional measurements, taken between each 2-hour cycle, indicated that creep was occurring throughout the test. After 8 to 10 hours of axial loading at 4000°R (2220°K), four of the six tabs failed. The tab failures are shown in figure 23.

Post-test inspection showed that

- (1) The holes in the tabs were greatly elongated in the axial direction, as shown in figure 24
- (2) Slight hole elongation occurred in the reinforced support tube
- (3) No pin deformation resulted
- (4) Pins at 4000°R (2220°K) under load bonded to the support tube and to the tabs at the areas of contact

Figure 25 shows bonding marks on a pin.

Failure in this test was caused by excessive creep in the tabs under the applied shear loading. In order to prevent such failures, the mechanical attachment must be modified. For example, the honeycomb tab thickness could be increased; however, increased tab thickness restricts the hydrogen propellant flow through the honeycomb passages which is not desirable. As an alternative, increased tab length would increase the shear area; thus, longer operation is possible.

This method of mechanical attachment might be better adapted for use on element stages near the reactor inlet where the drag loads are much lower and where the relative expansion between the honeycomb stage and the support tube is the greatest. The pin design allows such relative motion and may be well suited for this condition.

Metallurgical attachment evaluation. - The second attachment method was the metallurgical bond. The bond was achieved by the tungsten-vapor-deposition process discussed in reference 16. In the application of this process, the support tube is vapor deposited directly onto the previously formed fuel-element stages.

One metallurgical bond that was considered incorporated an unfueled tungsten ring as an integral part of the fuel-element stage, as shown in figure 26. Thin (0.020 in. (0.508 mm) thick) sacrificial molybdenum cylinders were slipped over each end of the fuel-element stage. The cylinders butted against the tungsten ring to form the plating surface or mandrel. Thus, the unfueled ring was the only exposed tungsten. The tungsten support tube was vapor deposited onto this surface attaching itself to the exposed tungsten ring. After the outside diameter of the support tube was machined to the desired dimension, the sacrificial molybdenum cylinders were leached out.

The attachment need not be a continuous band, as in the preceding case, but could consist of portions of a band, referred to as tabs in figure 27. This arrangement would have the advantage of increased support-tube flexibility during thermal cycling. Because of the convenience in specimen fabrication, portions of the outer periphery of a honeycomb stage, (fig. 28) were used as the surface on which to vapor deposit the tungsten. A bond of this type was achieved by machining six openings around the circumference of one thin molybdenum sleeve thus exposing the fuel stage in these areas. As the support tube was vapor deposited onto the sleeve, bonding to the fuel stage took place through the openings. Since the tungsten-vapor-deposition rate is uniform, the opening areas appear as depressions in the support tube. The deposition thickness must therefore be increased to allow the surface to be machined to a flush surface. After machining, the sacrificial molybdenum is leached out. If desired, a full-length fuel-element assembly consisting of 26 stages attached to a support tube could be fabricated by this method. For illustration, two phases of a two-stage subassembly are shown in figures 29 and 30. Normally, the fuel-element stages would be rotated 30° relative to each other to promote interstage gas mixing and to minimize uneven flow in the partial hexagonal passages at the periphery of the honeycomb. Molybdenum cylinders are added to each end of the molybdenum masking sleeves to extend the support tube and to cover the ends during the vapor-deposition process.

Elements of this type were tested at 4000°R (2220°K) under axial loads corresponding to a 25-percent overload from the reference-design drag load of 20 pounds (89 N). The test time for heating and cooling was identical with the mechanical attachment procedure. Five 2-hour cycles were run. Post-test inspection showed that the 0.020-inch-

thick (0.508 mm) tungsten-support tube pulled in 0.004 inch (0.102 mm) on the diameter at the six attachment windows. No pull-in was apparent 0.185 inch (4.76 mm) away from the point of attachment.

The test was repeated with an axial load of 50 pounds (222 N), 2.5 times the reference design load, which gave a shear stress of approximately 100 psi (69 N/cm²). The six bonds showed no evidence of failure, and the additional support tube pull-in was only 0.001 inch (0.0254 mm) for a total of 5 mils (0.127 mm) on the diameter. Ten thermal cycles were run totaling 20 hours of operation.

Results of Axial Supports

An axial support attachment consisting of six metallurgically bonded tabs withstood axial drag loads 2.5 times the maximum value calculated for reference-design conditions. In addition, the 0.020-inch-thick (0.508 mm) tungsten support tube, 5 mils (0.127 mm) thicker than the reference design, proved sufficiently flexible to accommodate the relative thermal expansion experienced in this test between the fueled honeycomb and the unfueled tungsten support tube. Ten thermal cycles were run totaling 20 hours of operation with no evidence of failure.

The mechanical attachment failed during a 5-cycle, 10-hour run when subjected to 1.25 times the maximum calculated drag load for the reference-design exit conditions. The type of failure experienced was such that a simple modification to the design would improve operating life.

Both attachment designs, the mechanical and the metallurgical, have advantages that compliment each other. Each design can be used to its best advantage. The mechanical pin attachment could be used at the reactor inlet to permit relative movement between the support tube and the hot fuel-element stage. At the inlet, the drag loads are low and the stresses in the attachment components are reduced.

For the tests conducted, the metallurgical attachment with its larger shear area proved stronger than the mechanical pin attachment as tested. The shear stress in the metallurgical attachment was approximately 100 psi (69 N/cm²) at the maximum load tested. Therefore, the metallurgical attachment might best be used at the reactor exit where the drag loads are the largest. In addition, the temperature difference between the fuel-element stage and the support tube is low at the reactor exit which minimizes the need for relative movement between the two.

Lateral Support Evaluation

The tungsten support tube, which holds the individual fuel-element stages, is fastened at the cold inlet end of the reactor. Other supports along the length are required to provide adequate stiffness for the support of lateral loads resulting from ground handling, chemical rocket boost, and in-flight maneuvers. The lateral support must transfer part of these loads from the support tube to the aluminum pressure tube.

In fulfilling the lateral support requirements, the support itself must not introduce additional problems. For example, lateral thermal expansion occurs between the hot tungsten support tube and the cold aluminum pressure tube. The lateral support must be able to accommodate this lateral expansion between the two tubes. In addition, the support must not provide a heat conduction path that would allow local overheating at the aluminum interface.

A thin tungsten corrugation, as illustrated in figure 27, could satisfy the requirements of a lateral support. Tungsten was chosen because it can withstand the high temperature of the support tube. A thin corrugation configuration should reduce the heat conduction through the lateral support in two ways. The thin cross section provides a small heat conduction path, and the corrugation increases the length of the heat conduction path over that of a radial support. In addition, whatever heat would be conducted through the support to the aluminum interface should be rapidly distributed because aluminum has such a high thermal conductivity. Thus, local overheating would be prevented at the aluminum interface. This latter problem is treated in reference 3.

Furthermore, for a given lateral support deflection caused by the relative thermal expansion in the annulus, the thinner the support, the less the bending stress. Thus, the chances for permanent support deformation are reduced. The desired support stiffness at the reduced stress level can be achieved by increasing the axial length of the support.

The stiffness of this lateral support is affected by the thickness of the material and the pitch of the corrugations. It is also desirable for a lateral support to provide uniform support regardless of the direction of the lateral disturbance. A 12-lobe corrugation made of tungsten sheet 5 mils (0.127 mm) thick was chosen.

In addition to providing the stated requirements, the corrugation may provide damping by frictional movement between the tubes and the corrugation lobes. This damping can prevent damaging vibrational amplitudes.

Tests were conducted to evaluate the tungsten corrugation as a lateral support. Two types of experiment were conducted: thermal expansion and lateral vibration.

Thermal expansion evaluation. - The amount of differential thermal expansion between the support tube and the aluminum pressure tube varies with axial position. The support tube temperature is approximately equal to the propellant temperature, which

increases as it passes through the reactor. The maximum support tube temperature in the region of the last stage is about 4000°R (2220°K). In contrast, the aluminum pressure tube cooled by the water moderator remains at a uniform temperature of approximately 760°R (422°K).

Tests were conducted at various combinations of temperature and differential thermal expansion to determine how well the 12-lobe corrugation could accommodate thermal expansion. The 5 mil (0.127 mm) thick corrugation was inserted between an outer tungsten cylinder with a 2.50-inch (6.35-cm) inside diameter and a tantalum inner cylinder with a 2.25-inch (5.72-cm) outside diameter. This arrangement (fig. 31) provides the required 0.125-inch (3.18 mm) annulus. In addition, the size of the tantalum ring approximates the support-tube outside diameter. The difference in thermal expansion coefficients between tungsten and tantalum provided relative expansion when the support test assembly was heated to a uniform temperature in a furnace.

The relative expansion between tungsten and tantalum at 4500°R (2500°K) produced a 5-mil (0.127 mm) radial decrease in the 0.125-inch (3.18 mm) annulus. If a condition simulating the relative expansion in the region of the last stage was desired, an additional 3-mil (0.0762 mm) radial decrease must be achieved. This additional 3-mil (0.0762 mm) annulus decrease was achieved by inserting 3-mil-thick (0.0762 mm) tungsten shim stock as room-temperature interference between the tungsten lobes and the inner tantalum ring.

The corrugated support is a structure fabricated from flat tungsten sheet. The individual lobes of the corrugated sheet were formed at elevated temperatures, and the ends of the corrugated sheet were stapled together forming a ring. Figure 32 shows a typical corrugation stapled together. Obviously this support structure, as fabricated, was not a precision piece of hardware. Even if it were, its inherent flexibility imposes a formidable task of determining lobe tolerances, whether the corrugation support is in or out of the annulus. Therefore, it was difficult to determine accurately the amount of decrease resulting from permanent set.

In discussing the results of thermal expansion furnace tests, listed in table I, the last column gives a realistic range of permanent set. Also shown in the table is the time at temperature and the number of thermal cycles.

In order to get the full significance of the data presented in the table, deflections must be associated with temperature levels. Note that at each temperature level, the total deflection consists of relative thermal expansion between the inner and outer rings plus any initial radial interference introduced by shimming. At temperatures lower than 3500°R (1945°K) no permanent set was apparent at a deflection of 2 mils (0.05 mm). The midcore axial position corresponds to a support tube operating temperature of 2000°R (1110°K). At this position, the relative expansion between the two tubes produces a 2-mil (0.05 mm) radial decrease in the 0.125-inch (3.18 mm) annulus. There-

fore, the conclusion from the results presented in table I is that the lateral support at the midcore position will not take a permanent set under the reference-design thermal-expansion operating conditions.

At the 4000° to 4500° R (2220° to 2500° K) temperature level, a 6-mil (0.15 mm) deflection indicates the possibility of a 1-mil (0.03 mm) permanent set. Still maintaining the 4000° to 4500° R (2220° to 2500° K) temperature level but imposing an 8-mil (0.20 mm) deflection, which is the relative expansion in the region of the last stage of the reference design, indicates the possibility of a 3-mil (0.08 mm) permanent set. Therefore, the 5-mil (0.127 mm) thick corrugation can be used in the region of the last stage but with the risk of permanent set.

The two remaining test temperatures of 4700° and 5000° R (2610° and 2780° K) were above the reference-design exit region temperature of 4000° R (2220° K), and at these elevated temperatures, permanent set definitely occurred. If clearances occur from permanent set, the lateral support may not provide effective support against vibrations. The seriousness of the clearances resulting from a permanent set is discussed in the following section.

Lateral vibration evaluation. - Evaluation of the lateral support requires a determination of the ability of the support itself to withstand the stresses imposed and the degree of stiffness it affords to reduce the deflections of the support tube. The stresses imposed were of concern because of the room temperature brittleness of tungsten which was chosen as the support material.

If the lateral corrugated support provides sufficient vibrational coupling or stiffness between the support and pressure tubes, the combination of support tube, corrugated support, and pressure tube will become more rigid and thus reduce the support tube bending stresses.

Another way to keep support-tube bending stresses low is to decrease deflection particularly at resonance by introducing damping. Damping can be viscous (proportional to velocity), solid (internal friction), or coulomb (sliding friction between dry surfaces). If the lateral support provides coupling between the two tubes, some viscous damping is obtained from the motion of the aluminum pressure tube in the surrounding water. This report on lateral support, however, is restricted to the damping resulting from the interaction between the corrugated spring and the two tubes. This damping would essentially be sliding-friction damping. The small deflections permissible and the thin corrugations to be used preclude any significant internal damping.

Evaluation of the lateral support included measurements of the stiffness in terms of static and dynamic spring constants and a determination of the ability of the support to operate in a vibrational mode without failure.

Determination of static spring constant: The static spring constant was measured in the conventional manner; a load was applied and the deflection was measured. Typical

static spring constants were obtained as the slope of the force against deflection curve. The apparatus is shown in figure 33. The load was transmitted to the corrugation by applying weights to both ends of a cylinder which rests inside a simulated fuel element. A dial gage was used on each end of the shaft to detect corrugation cocking and indicate spring deflection.

The corrugated spring, formed by stapling the ends of a corrugated sheet to form a ring, did not produce a uniform spring at the joint. Therefore, all static and dynamic tests were run with the joint at 90° to the direction of motion.

Load-deflection curves were obtained for several corrugations and varied from one corrugation to another depending on the precision of fabrication. A typical load-deflection curve for an 11-lobe corrugation is shown in figure 34. During the static spring constant measurements, the load was applied in small increments. Because the spring is stiff, the initial deflections are extremely small and difficult to measure accurately with the instruments used. However, after increasing the load to produce deflections of approximately 0.5 mil (0.0127 mm), the corrugations apparently slide along the tube walls and give additional larger deflections for corresponding load increments.

The curve indicates that the static spring constant is approximately 140 000 pounds per inch (2.445×10^5 N/cm) over the initial deflection range of zero to 0.25 mil (0.00635 mm). Beyond this deflection, corrugation slipping may occur, and the corrugation no longer behaves as a linear spring. The extent of the linear range can be expected to be dependent on the interference fit of the spring. Excessive interference would, however, increase the probability of a permanent set taking place at operating temperature.

Determination of dynamic spring constant: The model used to determine the vibration characteristics of the corrugated lateral support is the basic element of many vibration instruments. Figure 35 illustrates the schematic model and the actual test components corresponding to the model.

The instantaneous spring deflection is the relative displacement z between the absolute displacement y of the simulated fuel-element mass m and the absolute displacement x of the shake table. The analytical characteristics of the model for steady-state operation are represented by equation (5) which is derived in reference 17:

$$\frac{Z}{X} = \frac{\beta^2}{\sqrt{(1 - \beta^2)^2 + (2\zeta\beta)^2}} \quad (5)$$

where Z/X is the ratio of the maximum corrugation deflection to the maximum table displacement, β is the ratio of table frequency to undamped natural frequency of the

~~CONFIDENTIAL~~

spring mass system, and ζ is the damping factor (the ratio of equivalent viscous damping coefficient to critical damping coefficient).

Two 12-lobe tungsten corrugations were tested; one 3 mils (0.0762 mm) thick and one 5 mils (0.127 mm) thick. Either corrugation was inserted in the 0.125-inch (3.18 mm) annulus between the inner ring and the rigid test fixture, as shown in figure 35. The rigid clamping between the shake table and the test fixture enables one to assume that they are the same structure. The mass used in the model, as the inner ring, was chosen as 1.1 pounds (0.50 kg) to simulate the mass of an individual fuel-element stage. The choice of this mass does not affect the dynamic spring constant nor the equivalent viscous damping of the corrugation. Furthermore, this mass results in a resonant frequency within the desired frequency range. The corrugation and simulated fuel stage are shown in figure 31 and are 1.5 inches (3.81 cm) in the axial direction.

Tests were run at various table accelerations through a frequency range of 5 to 2000 cps (5 to 2000 Hz). The data taken were shake-table frequency, maximum table acceleration, and maximum mass acceleration. The original data points are shown in figures 36 and 37. Acceleration values are plotted in units of acceleration (g's). The data above 1400 cps (1400 Hz) were erratic. This irregular behavior existed in the shake table itself without the test equipment. Fortunately, this erratic behavior was far beyond the resonant frequencies of the corrugations tested. These data were used to obtain maximum relative displacements. Instantaneous spring deflections or relative displacements z and accelerations are given by the following equations:

$$z = (y - x) \quad (6)$$

$$x = X \sin \omega \tau \quad (7)$$

$$\frac{d^2 x}{d\tau^2} = -\omega^2 X \sin \omega \tau \quad (8)$$

$$y = Y \sin(\omega \tau - \varphi) \quad (9)$$

$$\frac{d^2 y}{d\tau^2} = -\omega^2 Y \sin(\omega \tau - \varphi) \quad (10)$$

where φ is the phase angle between the mass displacement and the driving force.

If the damping is small (approximately 10 to 15 percent of critical), the displacement and driving force are approximately in phase until resonance occurs. In the region of resonance, a phase shift occurs and the driving force and displacement changes from in-phase to 180° out of phase.

In order to determine the phase-angle shift, a test was conducted over the frequency range of interest with the shake table and mass accelerometer output displayed on a dual-beam oscilloscope. Twelve-lobe corrugations 3 and 5 mils (0.0762 and 0.127 mm) thick were run through a frequency range of 5 to 2000 cps (5 to 2000 Hz). In all cases, the phase shift was abrupt at resonance. Therefore, the phase angle ϕ was considered zero below resonance and 180° beyond resonance.

Equations (6) to (10) can accordingly be combined and rewritten with the appropriate phase angles to give the maximum relative displacement as follows:

$$Z = \frac{a_t}{\omega^2} - \frac{a_m}{\omega^2} \text{ for } \omega < \omega_n \quad (11)$$

$$Z = \frac{a_t}{\omega^2} + \frac{a_m}{\omega^2} \text{ for } \omega > \omega_n \quad (12)$$

The maximum spring deflections were obtained from these equations and figures 36 and 37 to yield the data presented in figure 38. The assumption of an instantaneous phase shift at resonance introduces a discontinuity in the deflection curve calculated from equations (11) and (12). Actually, there is a small frequency range on either side of resonance through which the phase shift occurs, which was disregarded in the simplified calculations. The size of this frequency range is dependent on the amount of damping present. In order to eliminate this discontinuity in Z , each curve in figure 38 was faired through the average of the values given by equations (11) and (12) at a frequency corresponding to the maximum value of a_m/ω^2 . The fairing through this point resulted in a maximum value of Z greater than that of the fairing point and at a slightly higher frequency. The error due to this fairing is deemed to be small.

The deflections are seen to be small and, except for the highest excitations at resonance, are within the linear range of the spring, as determined by the static load-deflection measurements.

The dynamic spring constant can be determined from a knowledge of the undamped natural frequency of the spring mass system or from the accelerations measured in the tests. The spring constant is given in terms of the undamped natural frequency according to the following equation:

$$\kappa = \omega_n^2 m = (2\pi f_n)^2 m \quad (13)$$

No measurements were made of the undamped natural frequency. This frequency was taken to be equal to the highest resonant frequency of the experimental curves for each corrugation. For example, the natural frequency for the 5-mil-thick (0.127 mm) corrugation was selected as 1250 cps (1250 Hz) from figure 37. This value and a mass of 1.1 pounds (0.50 kg) were used to compute the dynamic spring constant at resonance as 176 000 pounds per inch (3.08×10^5 N/cm). Similarly, the dynamic spring constant for the 3-mil-thick (0.0762 mm) corrugation was computed to be 40 500 pounds per inch (70 800 N/cm).

At this point, the dynamic spring constant is not established as independent of deflection and frequency. In order to evaluate the spring constant at points other than at resonance, equation (13) can be modified by multiplying and dividing by $\omega^2 Z$ and substituting a_t/X for ω^2 (see eq. (8)) to yield

$$\kappa = \frac{ma_t}{Z} \left(\frac{Z}{X\beta^2} \right) \quad (14)$$

If β is chosen to be far from resonance ($\beta = 0.4$), Z/X is insensitive to the damping factor when the damping factor is small ($0 < \zeta < 0.2$), as shown by equation (5). For these conditions, equation (5) gives $X\beta^2/Z$ equal to 0.85. Dynamic spring constants were computed from equation (14) at $\beta = 0.4$ by using values for a_t and Z from figure 38. The average values of κ obtained were 182 000 pounds per inch (3.185×10^5 N/cm) at 500 cps (500 Hz) for the 5-mil-thick (0.127 mm) corrugation and 51 300 pounds per inch (89 700 N/cm) at 240 cps (240 Hz) for the 3-mil-thick (0.0762 mm) corrugation. These values are summarized in table II.

The most important conclusion drawn from the table is that the corrugation is a stiff spring that provides the coupling between the two tubes. It is the small amount of damping, however, that prevents corrugation damage at resonance. In addition, the spring constant remains relatively constant over the deflection range covered. However, the spring constant is higher away from resonance. It may be possible that slipping at the higher deflections near resonance explains this effect.

Damping evaluation. - The amount of damping or the damping factor can best be shown by representing the data of figures 36 to 38 in the more conventional representation expressed analytically by equation (5). The values of Z/X were calculated from the Z values of figure 38 and the maximum shake-table displacement. These values are shown plotted in figure 39 as a function of frequency ratio.

Superimposed on the experimental Z/X curves are several analytical curves calculated from equation (5) for damping factors of 0.03, 0.05, and 0.10 for the 5-mil (0.127 mm) corrugation and 0.03, 0.10, and 0.15 for the 3-mil (0.0762 mm) corrugation (see fig. 39). Also added to figure 39 are the analytical Z/X values at resonance for a range of damping factors from 0.03 to 0.10. Viscous damping is proportional to velocity and lends itself to mathematical treatment. This is the main reason why it is convenient to express damping in terms of equivalent viscous damping. The similarity between the analytical and experimental curves (fig. 39) clearly indicates the range of damping factors for each corrugation. The similarity between the analytical and experimental curves show that the damping can be treated as viscous damping. The damping factor for the 5-mil (0.127 mm) corrugation does not exceed 0.08. Stated differently, the 5-mil (0.127 mm) corrugation has less than 8 percent of critical damping over the range of table excitation covered. The range of table excitation extended to 5.0 g's for the 5-mil (0.127 mm) corrugation and 3.5 g's for the 3-mil (0.0762 mm) corrugation. Similarly, the 3-mil (0.0762 mm) corrugation has less than 15 percent of critical damping.

In conclusion, the amount of damping is small, but true viscous damping does not exist. If true viscous damping did exist, the damping factor would be a constant, and only one curve would be required to represent each corrugation in figure 39. The experimental and analytical curves agree quite well because the amount of damping is small. At frequencies away from resonance, even though the damping factor varies along a given experimental curve, the effect of damping on Z/X is small.

Thus far, damping is discussed in terms of a damping factor which is dependent on the spring-mass system. In order to be able to apply the information to a general case, it is necessary to express the damping effect in terms of a damping coefficient which is independent of the mass. Although true viscous damping does not exist, an equivalent viscous damping coefficient may be used.

The equivalent viscous damping coefficient c can be calculated at the natural frequency by the following equation from reference 17:

$$c = \frac{ma_t}{Z_n \omega_n} \quad (15)$$

where ma_t is the impressed force. All the quantities of equation (15) were known from the tests conducted except c . This equation was used to calculate the equivalent viscous damping coefficient shown in figure 40, but only the resonant points were used to obtain these data. Therefore, frequency was not varied and the effect of frequency was not determined. Reference 17 states that when true viscous damping does not exist, the equivalent viscous damping coefficient will be a function of displacement and frequency.

Additional testing, for example with different masses, would be required to investigate the effect of frequency on the equivalent viscous damping of the corrugation. With the data available, the equivalent viscous damping coefficients can only be given as functions of displacement, as presented in figure 40. The equivalent viscous damping coefficients increase with increasing displacement for both corrugations. This effect would be expected if damping is associated with sliding of the corrugations which increases with displacement.

Clearance tests: During the dynamic tests, neither the 3- nor the 5-mil thick (0.0762 nor the 0.127 mm) corrugations had clearance when inserted into the annulus. In no instance did any of the corrugations crack or shatter.

Thermal expansion tests at temperatures as low as 4000°R (2220°K) showed a permanent set in the corrugation after thermal cycling. In order to determine if clearances create a problem area, shake tests were conducted with recrystallized corrugations that had radial clearances of 1 to 2 mils (0.0254 to 0.0508 mm). 5-mil-thick (0.127 mm) corrugations were subjected to 2-minute runs covering the frequency range from 5 to 2000 cps (5 to 2000 Hz). Each 2-minute run was made at a constant maximum table acceleration starting with 0.5 g, then 1 g, thereafter increasing in 1-g increments. After each test, the corrugation was checked for cracks with a dye penetrant. If no cracks were apparent, the test was run at a higher g-level. No failure occurred at table accelerations of 3 g's or less. Several corrugations cracked at 4 g's and above.

Lateral Support Results

The requirements of a lateral support for the fuel-element support tube were satisfied by a tungsten corrugated sheet placed in the annulus between the support tube and the aluminum pressure tube. Such a support was tested to evaluate its ability to accommodate thermal expansion and to determine its stiffness and damping characteristics when operating in a vibrational mode.

Test results of a 5-mil-thick (0.127 mm) corrugation showed that, at temperatures below 3500°R (1945°K), no detectable permanent deformation occurred from thermal expansion that produces a 2-mil (0.0508 mm) decrease in the annular space. Because a 2-mil (0.0508 mm) deflection at a temperature of 2000°R (1110°K) is expected in the reference design at the midcore position, the tungsten corrugation is acceptable at this location from the viewpoint of thermal expansion. A 5-mil-thick (0.127 mm) corrugation can only be used at temperatures greater than 3500°R (1945°K) and deflections greater than 2 mils (0.0508 mm) if a permanent deformation can be tolerated.

Vibration tests with a 1.1 pound (0.50 kg) mass showed no failure of the corrugations up to accelerations of 5 g's provided that no clearance exists between the corrugation and

~~CONFIDENTIAL~~

the tubes on either side of it. Spring constants were determined to range from 176 000 to 182 000 pounds per inch (3.08×10^5 to 3.185×10^5 N/cm) for a 5-mil-thick (0.127 mm) corrugation and from 40 000 to 51 000 pounds per inch (70 000 to 89 300 N/cm) for a 3-mil-thick (0.0761 mm) corrugation. This variation in spring constant is in agreement with the nonlinearity observed in the static spring deflection measurements. Equivalent viscous damping coefficients varied from 1 to 4 pound-second per inch (1.75 to 7.00 (N)(sec)/cm) over the range of displacement investigated. Damping was less than 8 percent of critical for the 5-mil-thick (0.127 mm) corrugation and less than 15 percent of critical for the 3-mil-thick (0.0762 mm) corrugation.

The corrugation is expected to provide a coupling between the support tube and pressure tube that is stiff enough to reduce support tube bending stresses to allowable values and flexible enough to accommodate thermal expansion.

Lewis Research Center,
National Aeronautics and Space Administration,
Cleveland, Ohio, July 27, 1967,
122-28-02-04-22.

~~CONFIDENTIAL~~

APPENDIX A

SYMBOLS

A	flow area	k	thermal conductivity
a	maximum acceleration	L	heated length of reactor flow passage
B	heat transfer surface area per unit volume	l	axial distance from reactor inlet
b	fueled material thickness	M	Mach number
C	constant, product of Stephan-Boltzmann constant and emissivity	m	mass
C_1, C_2, C_3, C_4	constants of integration	N	$(q'''/k) + n(T_b - T)$
c	equivalent viscous damping coefficient	n	hB/k
c_p	specific heat at constant pressure	P	total pressure
D	equivalent diameter	Pr	Prandtl number
E	Young's modulus of elasticity	p	static pressure
f	friction factor	\bar{p}	average static pressure in reactor core, $(p_i + p_o)/2$
f	frequency	Q	$\sqrt{2u^2h/k_wb}$
G	mass velocity, flow rate per unit area	q''	heat flux
g	acceleration of gravity	q'''	heat-generation rate per unit volume
H	perimeter	R	gas constant
h	heat-transfer coefficient	Re	Reynolds number, DG/μ_s
$I_0(r\sqrt{n})$	modified Bessel function of zero order, first kind	r	radius
$K_0(r\sqrt{n})$	modified Bessel function of zero order, second kind	S	surface area
K	ratio of heat-generation rates	s	distance in direction of conductive heat flow
		T	temperature, absolute units
		T_b	total bulk fluid temperature, absolute units

T_s	surface temperature, absolute units	λ	volume fraction of UO_2 in fuel-element material
\bar{T}	average gas temperature, $(T_i + T_o)/2$	μ	viscosity
t	static fluid temperature, absolute units	ν	Poisson's ratio
u	one-half width of web (see fig. 14)	ρ	density
V	volume	σ	stress
v	velocity	φ	phase angle between driving force and mass displacement, radi
w	weight flow rate	ω	angular speed
X	maximum table displacement	τ	time
x	instantaneous table displacement	ϵ	unit strain
Y	maximum mass displacement	Subscripts:	
y	instantaneous mass displacement	b	bulk
Z	maximum relative displacement	c	critical
z	instantaneous relative displacement	i	reactor inlet propellant
α	linear coefficient of expansion	m	mass
β	frequency ratio, $\omega/\omega_n = f/f_n$	n	natural undamped
γ	ratio of specific heat at constant pressure to specific heat at constant volume	net	net
ζ	damping factor, c/c_c	o	reactor outlet propellant
η	fractional distance, s/u	p	periphery of cylindrical fuel element
θ	temperature parameter, $2h(T - T_b)/q''b$	s	surface
κ	spring constant	t	table
		w	web
		$0, 1, \infty$	value of η , refers to position, (fig. 14)
		$2, 3, 4$	radial position (fig. 44)

~~CONFIDENTIAL~~

APPENDIX B

AXIAL PROPELLANT TEMPERATURE DISTRIBUTION

The variation of propellant temperature as a function of axial distance from the reactor inlet is derived herein for the case of constant axial surface temperature. The derivation is intended to determine the length to diameter ratios required to achieve a prescribed outlet temperature for the purposes of a parametric study. Certain approximations are made to simplify the derivation which are considered to be adequate for the intended purpose.

The axial variation of coolant gas temperature for a constant axial surface temperature can be derived as follows:

A heat balance on an axial element gives

$$q'' H dl = w(c_p)_b dT \quad (B1)$$

From the definition of the heat-transfer coefficient

$$q'' = h(T_s - T)$$

equation (B1) becomes

$$\frac{hH}{w(c_p)_b} dl = \frac{dT}{T_s - T} \quad (B2)$$

Using the definition of mass velocity G and equivalent diameter D gives equation (B2) in the form

$$\frac{4h}{G(c_p)_b} \frac{dl}{D} = \frac{dT}{T_s - T} \quad (B3)$$

Heat-transfer correlations appear in the literature in which the fluid properties are evaluated at surface, film, or bulk temperatures. Because integration of equation (B3) is to be performed, it is desirable to use a correlation equation with invariant properties. For the case of constant surface temperature, such an equation is

$$\frac{hD}{k_s} = 0.021 \left(\frac{DG}{\mu_s} \right)^{0.8} (\text{Pr}_s)^{0.4} \left(\frac{T}{T_s} \right)^{0.8} \quad (\text{B4})$$

which is similar to that of reference 18. Combining equations (B3) and (B4) gives

$$\frac{0.084}{\text{Re}_s^{0.2} \text{Pr}_s^{0.6}} \frac{(c_p)_s}{(c_p)_b} \left(\frac{T}{T_s} \right)^{0.8} \frac{dl}{D} = \frac{dT}{T_s - T}$$

Neglecting the variation in specific heat yields

$$\frac{dT}{T_s - T} = \frac{0.084}{\text{Re}_s^{0.2} \text{Pr}_s^{0.6}} \left(\frac{T}{T_s} \right)^{0.8} \frac{dl}{D} \quad (\text{B5})$$

Closed-form integration of equation (B5) can be performed if the temperature ratio exponent is taken as 1. This simplification results, however, in a heat-transfer coefficient h lower than it should be. The error introduced can be partly compensated for by using a larger coefficient.

Integration of equation (B5) with the temperature ratio exponent equal to 1 and an unknown coefficient C_0 yields:

$$\frac{C_0}{\text{Re}_s^{0.2} \text{Pr}_s^{0.6}} \frac{l}{D} = \ln \left[\frac{(T_s/T_i) - 1}{(T_s/T) - 1} \right] \quad (\text{B6})$$

The axial variation in propellant temperature resulting from equation (B6) is compared in figure 41 with the variation resulting from numerical integration of equation (B5). The comparison is made for the following case:

Constant surface temperature, T_s/T_i	16.67
Surface Reynolds number, Re_s	20 000
Prandtl number, Pr	0.7

Equation (B5) is represented by the solid line and deviates from a straight line. Equation (B6) is represented by dashed lines for two values of the constant C_0 : a value of 0.084 from equation (B5) and a larger value of 0.103. Increasing the constant in equation (B6) substantially corrects for the error introduced by taking the temperature ratio

exponent equal to 1. A value for C_0 of 0.103 was chosen to give the L/D corresponding to that resulting from equation (B5) for a nuclear rocket with $T_s/T_o = 1.111$. Equation (B6) thus becomes:

$$\frac{0.103}{Re_s^{0.2} Pr_s^{0.6}} \frac{l}{D} = \ln \left[\frac{(T_s/T_i) - 1}{(T_s/T) - 1} \right] \quad (B7)$$

The assumptions involved in the derivation of equation (B7) are not sufficiently correct to permit accurate calculation of axial heat flux variations for the constant surface temperature case. Equation (B7) will correctly determine, within the limits of equation (B5), the L/D required for the temperature ratios of interest for the nuclear rocket and will prescribe propellant temperature variations suitable for the pressure-drop calculations.

APPENDIX C

REACTOR CORE PRESSURE DROP

The pressure drop in a constant area duct is the sum of the friction and momentum pressure drops given by

$$dp = -4f \frac{\rho v^2}{2g} \frac{dl}{D} - \frac{\rho v}{g} dv$$

or written in terms of the mass velocity G

$$dp = -4f \frac{G^2}{2g\rho} \frac{dl}{D} - \frac{G}{g} dv \quad (C1)$$

From continuity and the equation of state for a perfect gas,

$$v = \frac{G R t}{p}$$

and

$$dv = GR \left(\frac{dt}{p} - t \frac{dp}{p^2} \right)$$

Equation (C1) then becomes

$$dp = - \frac{2fG^2 R t}{gpD} \frac{dl}{D} - \frac{G^2 R}{gp} \frac{dt}{D} + \frac{G^2 R t}{gp^2} dp \quad (C2)$$

which can be written as

$$p dp(1 - \gamma M^2) = - \frac{G^2 R}{g} \left(\frac{2ft}{D} \frac{dl}{D} + dt \right) \quad (C3)$$

For low Mach numbers, the term γM^2 and the difference between total and static temperatures can be neglected to give

$$p \, dp = - \frac{G^2 R}{g} \left(\frac{2fT \, dl}{D} + dT \right) \quad (C4)$$

The friction factor f is taken to be correlated in terms of Reynolds number similar to that of reference 19 according to

$$f = \frac{0.046}{Re_s^{0.2}} \quad (C5)$$

and is therefore independent of l . Combining equations (C4) and (C5) with T as a function of l given by equation (B7) from appendix B gives

$$p \, dp = - \frac{G^2 R}{g} \left(0.893 \, Pr_s^{0.6} \, T_s \frac{dT}{T_s - T} + dT \right)$$

This equation can be integrated in closed form to yield

$$\frac{p_i - p_o}{p_o} = \left\{ \frac{1 + 2G^2 R T_s}{g p_o^2} \left[0.893 \, Pr_s^{0.6} \ln \left(\frac{T_s - T_i}{T_s - T_o} \right) + \frac{T_o - T_i}{T_s} \right] \right\}^{0.5} - 1 \quad (C6)$$

The pressure drop calculated from equation (C6) is only applicable to low Mach number conditions mainly because of neglecting the term γM^2 of equation (C3). The simplification is equivalent to assuming constant pressure in the expression for dv in the momentum pressure drop. For the case of interest here, the momentum pressure drop is primarily caused by temperature rise and secondarily by pressure decrease. The applicable Mach number range can therefore be extended by augmenting the pressure drop calculated from equation (C6) by the last term in equation (C2) for average conditions. Applying this correction yields the following equation for overall pressure drop

$$\frac{p_i - p_o}{p_o} = \frac{\left\{ 1 + \frac{2G^2 R T_s}{g p_o^2} \left[0.893 \, Pr_s^{0.6} \ln \left(\frac{T_s - T_i}{T_s - T_o} \right) + \frac{T_o - T_i}{T_s} \right] \right\}^{0.5} - 1}{1 - \frac{G^2 R \bar{T}}{g \bar{p}^2}}$$

where \bar{p} is evaluated by first assuming the denominator to be equal to 1.

APPENDIX D

APPARATUS AND PROCEDURE FOR ROOM-TEMPERATURE FLOW TESTS

Apparatus Description

The apparatus used for the cold-flow tests may be conveniently described in three groups: the piping system, the test specimen holder, and the instrumentation.

Piping System

The parts of the piping system are shown in figure 42. The end connections are made at the inlet with 4-inch (10.2 cm) pipe to the 450-psi (310 N/cm²) laboratory air supply, and at the outlet with 6-inch (15.2 cm) pipe to the atmosphere outside the laboratory building. Within this pipe system, the air flows through the orifice section, the inlet control valve, the test section, and the exit control valve.

Immediately downstream of the inlet connection is a standard ASME orifice section for measuring the air flow rate.

To control both pressure level and flow rate, valves were placed both upstream and downstream of the test section (fig. 42). These valves were remotely operated from the control panel.

The test section was stationed between two pipe tees (fig. 42), each of which contained a sight glass to permit illumination and/or observation of the test piece. The specimen mounting section consists of two transparent plastic spool pieces each about 1 foot (30.5 cm) long, with the test assembly mounted to one of them.

Test Specimen Holders

All the concentric ring elements had two main support combs. The ends of these combs were fitted into notches in a steel cylinder (fig. 10(c)). This cylinder was, in turn, inserted into a holder with the upstream corners rounded to reduce entrance effects. This holder extended 0.75 inch (1.90 cm) upstream of the test element. The holder was attached to the mounting section.

Figure 6 shows the plate holder assembly for the single flat plate tests. This holder included a section 7.75 inches (19.7 cm) long upstream of the plate to develop the flow before reaching the upstream edge of the plate being tested. The flow passage surfaces were painted flat black to reduce light reflections.

Two features of the holder can be seen in figure 6(a). One is the contact point which was used to indicate a plate failure electrically. This contact is located 0.0625 inch (1.59 mm) downstream from the upstream edge of the plate, as shown. The other feature is a 0.03125-inch-diameter (0.794 mm) static-pressure tap, perpendicular to the surface and 0.5 inch (1.27 cm) upstream of the upstream edge of the plate.

Figure 43 is an enlarged edged view of the plate holder showing a typical spacer arrangement. The flow passage is formed by the 0.064-inch-thick (1.62 mm) spacers. The 0.0015-inch-thick (0.0381 mm) shims provide clearance so as not to clamp the plate in position.

Instrumentation

Four types of instrumentation provided the data required from these tests: pressure, temperature, optical, and electrical.

Pressure. - Static pressure taps were placed at four locations: two in the orifice flanges, one upstream of the test element and one immediately downstream of the test element. Calibrated pressure gages indicated upstream orifice pressure and upstream test plate pressure. Mercury manometers indicated pressure drop across the orifice plate and test element.

Temperature. - Iron-constantan thermocouples were used at two locations (fig. 42) to measure orifice air temperature and test section inlet temperature. These temperatures were indicated on a null-type potentiometer.

Optical. - The optical system (fig. 42) for the concentric-ring tests provided illumination of the ends of a test element with spotlights shining through the transparent spool pieces. The image of the ends was then transmitted by way of the sight glasses, mirrors, lens, and half-silvered mirror to the television and motion-picture cameras. There, both ends could be viewed and photographed simultaneously.

For the single-plate tests, the long narrow passage would not permit illumination in this manner. Instead, a light was placed at one sight glass and the cameras with lens and half-silvered mirror were placed at the other sight glass. This way, a silhouette of the single test plate could be observed and recorded. The image appeared to be similar to that shown in figure 6(b).

Electrical. - Micrometer-adjusted electrical contacts were provided in the plate holder assembly for indication of plate failure (preset deflection). These contacts were connected to an ohmeter.

Procedure

Testing. - The test plate or element was installed in its holder. The holder was inserted into the test section spool piece (fig. 42). All flange joints were pressure checked.

The test was started by opening the inlet control valve and setting the desired pressure level with a small gas flow rate. At this condition, a data point was taken for reference and the motion-picture camera was turned on. While maintaining constant pressure, air flow rate was then slowly increased until first contact was indicated between the test plate and the micrometer-adjusted electrical contact, or until visual and/or pressure indication showed element failure. Any one of these three conditions represented the failure condition, and data were recorded. The elapsed time during test was usually about 2 minutes.

Data reduction. - The air flow rate w was measured by using a standard ASME orifice run and orifice plates. With the flow rate known, the velocity was determined from the continuity equation, and the critical dynamic pressure $\rho v^2/2g$ was calculated.

The critical values of velocity and dynamic pressure are those evaluated at the flow rate producing plate failure. The air density and flow area are evaluated at the test plate or element.

~~CONFIDENTIAL~~

APPENDIX E

APPARATUS AND PROCEDURE FOR HOT-FLOW TESTS

Flow System

Hydrogen or helium was supplied from a tube trailer at a maximum pressure of 2400 psi (1660 N/cm^2). The gas flowed from the trailer through an on-off valve, a remotely operated flow-control valve, a choked-flow nozzle, and into the heater. The heater was composed of four sets of tungsten flat-plate heater elements. A detailed description of a typical set of heater elements is given in reference 20. Each of the four sets of heaters is individually controlled by saturable reactors and then rectified to direct current by silicon rectifiers. The gas flowed from the heater, through the test section and into a gas-to-water heat exchanger where it was cooled below 960° R (534° K) before being exhausted into the atmosphere.

For safety purposes, the entire system was purged with nitrogen before hydrogen entered the system, and the controls were set for fail-safe operations so that if a predetermined safety permissive stops the hydrogen flow, nitrogen would automatically purge the system. In such a case, the electrical heater power would also be automatically shut down.

Test Section

Experiments were performed on a test section consisting of a single tungsten flat plate 0.020- by 2- by 2-inch (0.508 mm by 5.08 cm by 5.08 cm) mounted in a boron nitride flow channel (fig. 8). The channel gap on either side of the plate was 0.060 inch (1.52 mm). The ends of the plate were held by molybdenum inserts. One end of the plate was clamped between these inserts. A pin passing through the inserts and the plate also served to hold the plate in position. Clearance was provided at the opposite end of the plate to permit the plate to slide and thus allow for thermal expansion.

Instrumentation

Molybdenum probes threaded into the boron nitride housing, one on each side of the plate, protruded through the channel wall at the leading edge and midspan of the plate (fig. 8). When contact between the probe and the plate occurred, an electrical circuit was completed and indicated on a resistance measuring device. Although provision for

~~CONFIDENTIAL~~

probes at three different positions along the plate in the flow direction was made, only the leading edge probe was used after initial testing. Because of the relatively short length of the plate in the flow direction, local deflection was not a problem, and bending was nearly uniform. For this reason, probes at the other locations were not necessary. A plate failure indication showed a sudden decrease in resistance and remained at essentially a short circuit.

The static pressure at the test section was measured by a temperature-compensated strain-gage-bridge pressure transducer located near the upstream edge of the plate. The gas temperature at the test section was determined from a thermocouple measurement of the gas temperature out of the heat exchanger and the amount of heat transferred to the water in the heat exchanger. To verify this method of temperature determination, the hot gas temperature was measured directly for several operating points.

~~CONFIDENTIAL~~

~~CONFIDENTIAL~~

APPENDIX F

CALCULATION OF EXPERIMENTALLY INDUCED TEMPERATURE PROFILE

The thermal stress experiment induces a radial temperature gradient in a honeycomb fuel element. A method is presented for calculating the temperature profile by using information available from the experiment. Temperature gradients are induced by heating the center portion of the honeycomb and cooling the outer surface with flowing gas. Between the heated and cooled areas is a no-flow zone (fig. 44). The metal temperature may be calculated from temperature and flow rate of the heating gas and from the temperature measurements made in the cooler no-flow zone. The analysis is similar to that presented in the section Radial temperature profile.

The honeycomb was considered to be a homogeneous circular cylinder with the thermal characteristics of the honeycomb. Within the no-flow zone, heat was transferred by conduction. In the experiment, thermocouples measure the temperature at two different radii. The temperature within the no-flow zone may be calculated from

$$\frac{T - T_4}{T_3 - T_4} = \frac{\ln(r_4/r)}{\ln(r_4/r_3)} \quad (F1)$$

This is the temperature relation for radial heat conduction through a cylinder without internal heat generation. Thermal conductivity was assumed to be a constant. The temperatures T_3 and T_4 are measured at radial locations r_3 and r_4 . Equation (F1) shows that the heat load need not be known in order to determine the radial temperature profile in the no-flow region.

In the center zone, heat is convected from the hot gas and conducted to the cooler zone. The 19 center hexagons are approximated by a cylinder with the same volume and porosity as the honeycomb. A heat balance of this zone gives the following differential equation:

$$\frac{d^2T}{dr^2} + \frac{1}{r} \frac{dT}{dr} + \frac{hB}{k} (T_b - T) = 0$$

This equation is identical to equation (3) of the section Radial temperature profile. The general solution is

$$N = C_1 I_0(r\sqrt{n}) + C_2 K_0(r\sqrt{n}) \quad (F2)$$

~~CONFIDENTIAL~~

where $n = hB/k$ and $N = n(T_b - T)$. The constant C_2 must be equal to zero in order that $dT/dr = 0$ at $r = 0$. The constant C_1 may be calculated from equation (F2) with $T = T_2$ at $r = r_2$:

$$C_1 = \frac{n(T_b - T_2)}{I_0(r_2 \sqrt{n})}$$

The temperature within the heated zone is then

$$T = T_b - \frac{(T_b - T_2)I_0(r \sqrt{n})}{I_0(r_2 \sqrt{n})} \quad (F3)$$

The temperature within the hot zone is a function of T_2 , T_b , h , and k . The temperature T_2 is calculated from equation (F1) at $r = r_2$. The heat-transfer coefficient h may be calculated if the hot-gas flow rate and temperature T_b are known. The value of the thermal conductivity k is discussed in the section Radial temperature profile.

When calculating the temperature profile as outlined, the temperature gradient at r_2 was not utilized as a boundary condition for the heated zone. A check on the calculated profile can be made by a comparison of the temperature gradients at r_2 from equations (F1) and (F3). Any discontinuity in slope dT/dr at this point is an indication of one or more of the following: (1) the temperature or flow measurements were in error, (2) the value of effective thermal conductivity was in error, (3) the conditions assumed for the calculations did not duplicate the test conditions, or (4) the heat-transfer model did not represent the honeycomb tested.

Calculations made for the tests discussed in the body of this report showed some discontinuity in the temperature gradient for all cases. Consideration of the errors in experimental measurements could not account for the discrepancy. Therefore items (3) and (4) were suspect. Because the analysis is based on radial heat conduction, any axial conduction in the test element would introduce an appreciable error if its contribution were of the same order or greater than the radial conduction. No measurements of axial temperature variation had been made to check on this item. A check was made, however, on the heat-transfer model by comparing the temperature profile obtained from the model (eqs. (F1) and (F3)) to results from an existing numerical program. The program was limited to nine hexagons across the diameter.

The numerical program uses a relaxation method with the area divided into nodes. A heat-transfer coefficient, gas temperature, and outer surface temperature were specified. The problem was divided into two zones. In the center zone, heat was transferred

by conduction and convection. In the outer zone, the only mode of heat transfer was conduction. Thus, the heat-transfer coefficient was set equal to zero in the outer zone. The temperature of each web was calculated and plotted as circles in figure 45.

A temperature profile was also calculated by using equations (F1) and (F3). Two radial temperatures are measured in the conduction zone during the experiment. Therefore, two temperatures calculated by the numerical program were selected as T_3 and T_4 for use in equation (F1) in order to check the application of the method. The interface temperature T_2 was calculated. The heat-transfer coefficient and gas temperature had been specified. The temperature profile in the heated zone was calculated by using equation (F3). The calculated temperature profile obtained from equations (F1) and (F3) is shown as a solid line in figure 45. There is good agreement between the two methods. It can therefore be concluded that the temperature can be calculated accurately by using a homogeneous model if the heat flow is radial.

~~CONFIDENTIAL~~

REFERENCES

1. Rom, Frank E.; Johnson, Paul G.; and Hyland, Robert E.: Water-Moderated Nuclear Rockets. NASA TM X-482, 1961.
2. Lietzke, Armin F.: Water-Moderated Tungsten Nuclear Rocket Reactor Concept. NASA TM X-1044, 1965.
3. Krasner, Morton H.: Feasibility Study of a Tungsten Water-Moderated Nuclear Rocket. V. Engine System, NASA TM X-1424, estimated publication, approximately, Jan. 1968.
4. Ribble, Guy H.: Feasibility Study of a Tungsten Water-Moderated Nuclear Rocket. VI. Feed System and Rotating Machine. NASA TM X-1425, estimated publication, approximately, Jan. 1968.
5. Saunders, Neal T.; Gluyas, Richard E.; and Watson, Gordon K.: Feasibility Study of a Tungsten Water-Moderated Nuclear Rocket. II. Fueled Materials. NASA TM X-1421, estimated publication, approximately, Jan. 1968.
6. Klann, Paul G.; Mayo, Wendell; Lantz, Edward; and Paulson, Walter A: Feasibility Study of a Tungsten Water-Moderated Nuclear Rocket. IV. Neutronics. NASA TM X-1423, estimated publication, approximately, Jan. 1968.
7. Thornton, G.; Minnich, S. H.; and Heddleson, C. H.: Heat Transfer Reactor Experiment No. 1. Rep. No. Apex-904, General Electric Co., Feb. 28, 1962.
8. Cook, R. G.; Goldstein, M. B.; Moon, C. W.; and Prickett, W. Z.: Gas-Cooled High-Temperature Nuclear Reactor Design Technology. 4. Cellular Metallic Fuel Reactors. Rep. No. APEX-800, Part B, General Electric Co., June 30, 1962.
9. Miller, D. R.: Critical Flow Velocities for Collapse of Reactor Parallel-Plate Fuel Assemblies. J. Eng. Power, vol. 82, no. 2, Apr. 1960, pp. 83-95.
10. Brown, Ronald D.; and Levin, L. Ross: A 6-Inch Subsonic High-Temperature Arc Tunnel for Structures and Material Tests. NASA TN D-1621, 1963.
11. Schmidt, F. F.; and Ogden, H. R.: The Engineering Properties of Tungsten and Tungsten Alloys. DMIC Rep. 191, Battelle Memorial Inst., Sept. 27, 1963. (Available from DDC as AD-425547).
12. Jakob, Max: Heat Transfer. Vol. I. John Wiley and Sons, Inc., 1949, p. 185.
13. Timoshenko, S.; and Goodier, J. N.: Theory of Elasticity. Second ed., McGraw-Hill Book Co., Inc., 1951, p. 410.

~~CONFIDENTIAL~~

14. Sikora, Paul F.; and Blankenship, Charles P.: Evaluation of Processes for Fabricating Tungsten - Uranium Dioxide Honeycomb Configurations. NASA TM X-1445, 1967.
15. Spanner, J. C.; and Brown, R. L., Jr.: Development of Nondestructive Testing Methods for NASA Tungsten, Water-Moderated Reactor Fuels. Vol. II-Test Methods and Equipment Summary. Rep. No. BNWL-384 (NASA CR-72140), Battelle Northwest, Apr. 1967.
16. Perkins, K. M.; Legacy, D. J.; Thompson, W. H., Jr.; and Maeyens, E., Sr.: Tungsten Vapor Deposition for Reactor Component Fabrication. Rep. No. Y-12 Y-PG-629 (NASA CR-72067), Union Carbide Corp., Nov. 10, 1966.
17. Thomson, W. T.: Mechanical Vibrations. Second ed., Prentice-Hall, Inc., 1953.
18. Humble, Leroy V.; Lowdermilk, Warren H.; and Desmon, Leland G.: Measurements of Average Heat-Transfer and Friction Coefficients for Subsonic Flow of Air in Smooth Tubes at High Surface and Fluid Temperatures. NACA Rep. 1020, 1951.
19. McAdams, William H.: Heat Transmission. Third ed., McGraw-Hill Book Co., Inc., 1954.
20. Slaby, Jack G.; Maag, William L.; and Siegel, Byron L.: Laminar and Turbulent Hydrogen Heat Transfer and Friction Coefficients over Parallel Plates at 5000° R. NASA TN D-2435, 1964.

~~CONFIDENTIAL~~

~~CONFIDENTIAL~~

TABLE I. - THERMAL EXPANSION OF 5-MIL (0.127 MM)

12-LOBE CORRUGATION

Number of cycles	Time per cycle, min	Temperature		Initial radial inter- ference, mils	Total radial deflection, temperature plus shims		Approximate permanent radial set	
		°R	°K		mils	mm	mils	mm
2	15	3500	1945	0	2	0.05	0	0
	15	4000 to 4500	2220 to 2500	1	6	.15	0 to 1	0 to 0.03
		15	4000 to 4500	2220 to 4500	3	8	.20	0 to 3
1	15	4700	2610	5	11	.28	6 to 7	0.15 to 0.18
5	10	5000	2780	0	8	.20	4 to 5	0.10 to 0.13

TABLE II. - VIBRATION CHARACTERISTICS

OF CORRUGATED SPRING

[Number of lobes, 12; corrugation length, 1.5 in. (3.81 cm); mass, 1.1 lb (0.50 kg).]

Characteristic	Corrugation thickness	
	5 mil (0.127 mm)	3 mil (0.0762 mm)
Natural frequency, cps (Hz)	1250	600
Spring constant at frequency ratio of 1, lb/in. (N/cm)	176 000 (308 000)	40 500 (70 800)
Spring constant at frequency ratio of 0.4, lb/in. (N/cm)	182 000 (318 500)	51 300 (89 700)
Damping factor at excitation of		
0.5 g	0.03	0.04
3.5 g's	----	.15
5 g's	.08	----

~~CONFIDENTIAL~~

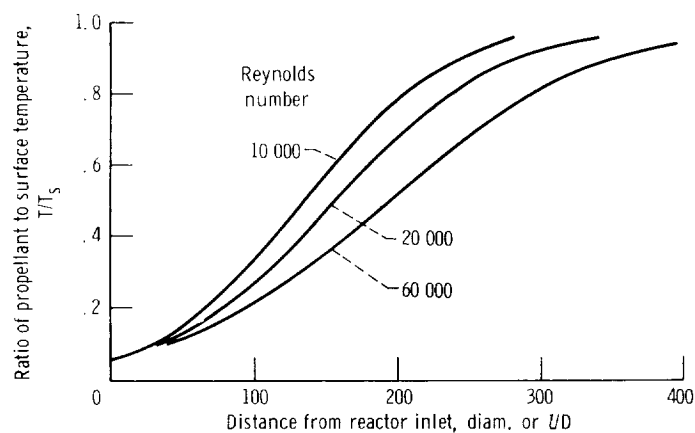


Figure 1. - Axial variation of propellant temperature. Constant surface temperature, $T_s/T_i = 16.67$.

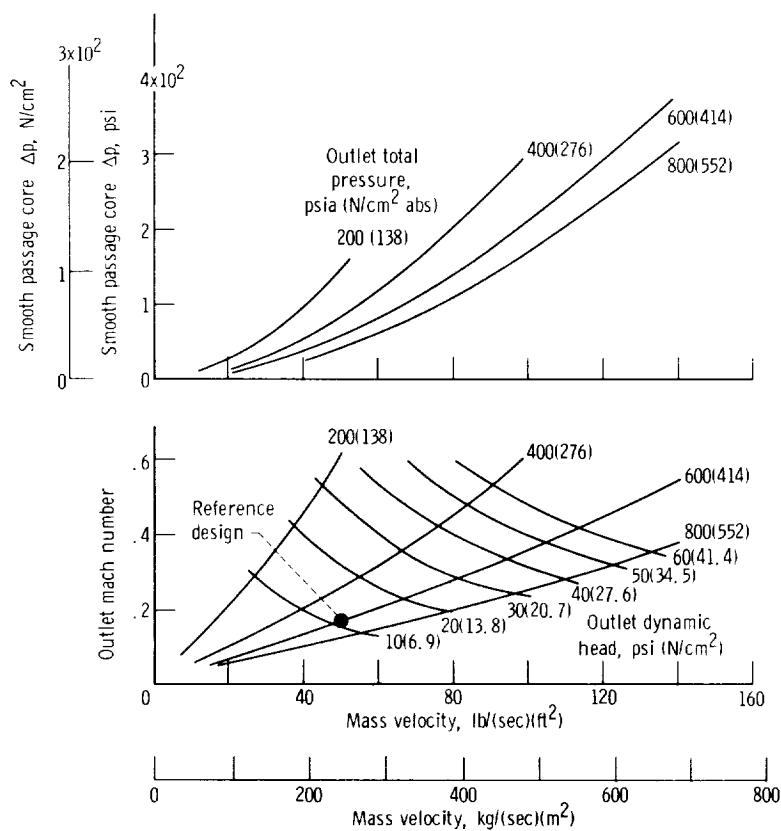
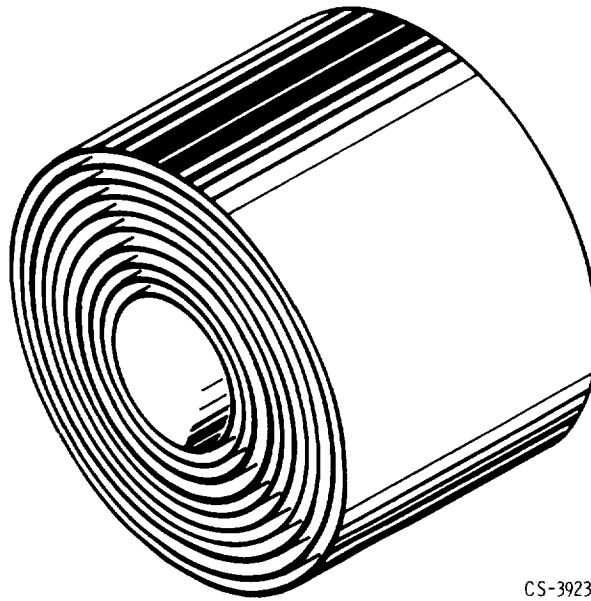
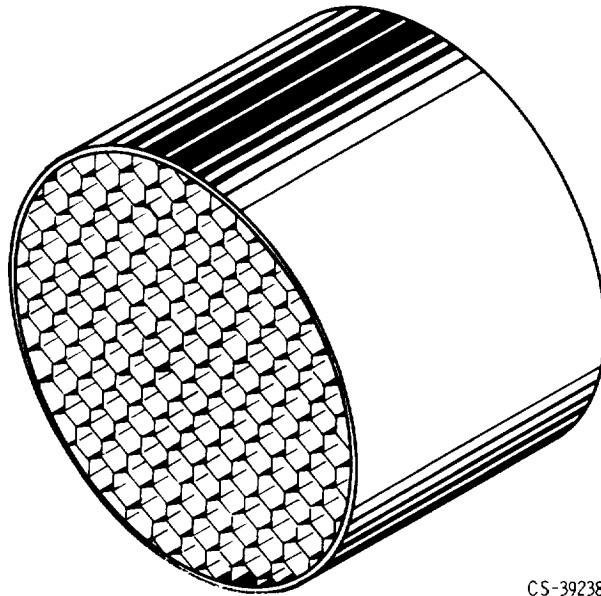


Figure 2. - Interrelation of operating parameters.



CS-39237

Figure 3. - Concentric-cylinder configuration.



CS-39238

Figure 4. - Honeycomb configuration.

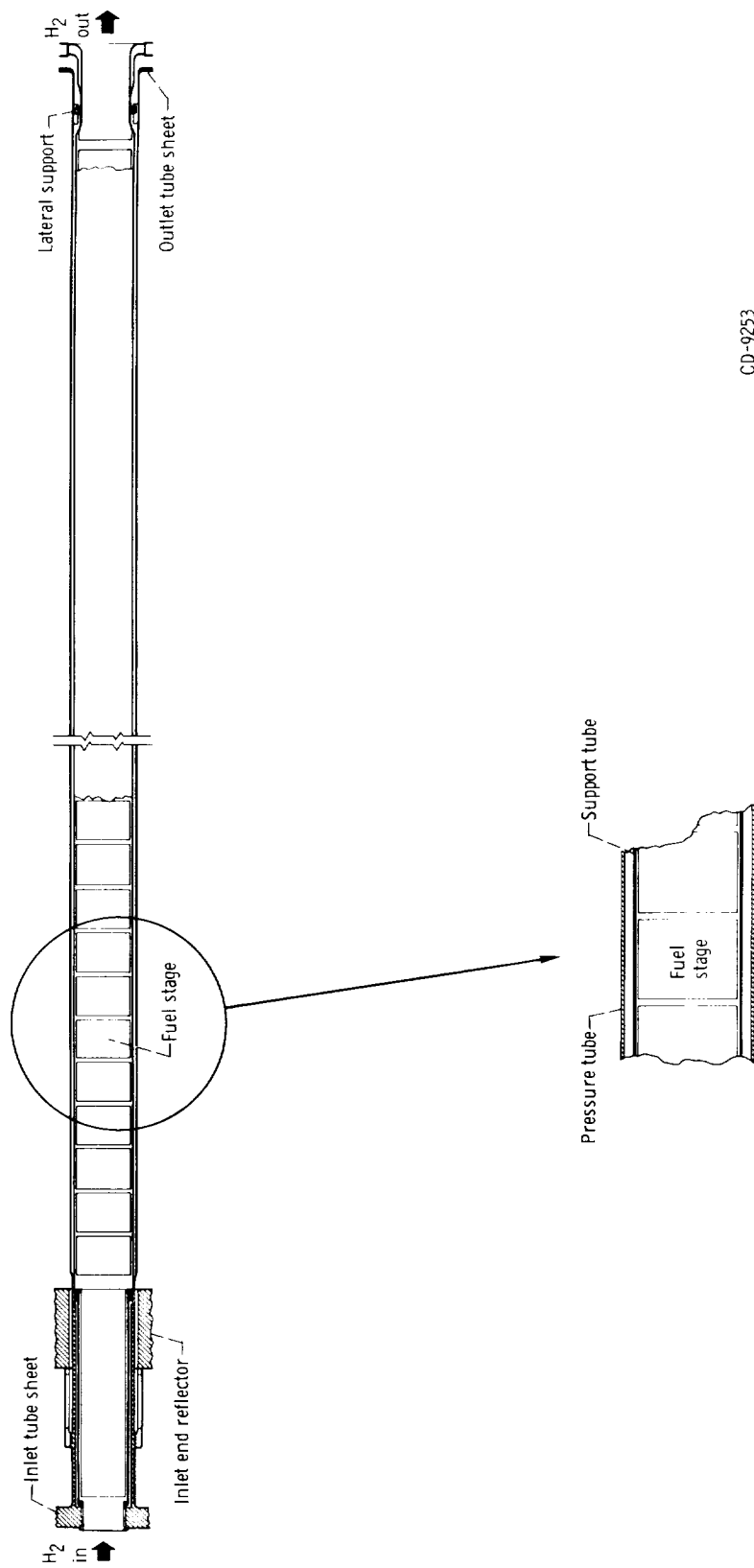
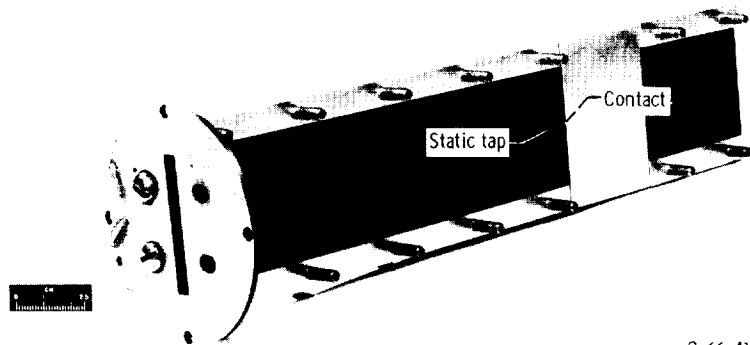


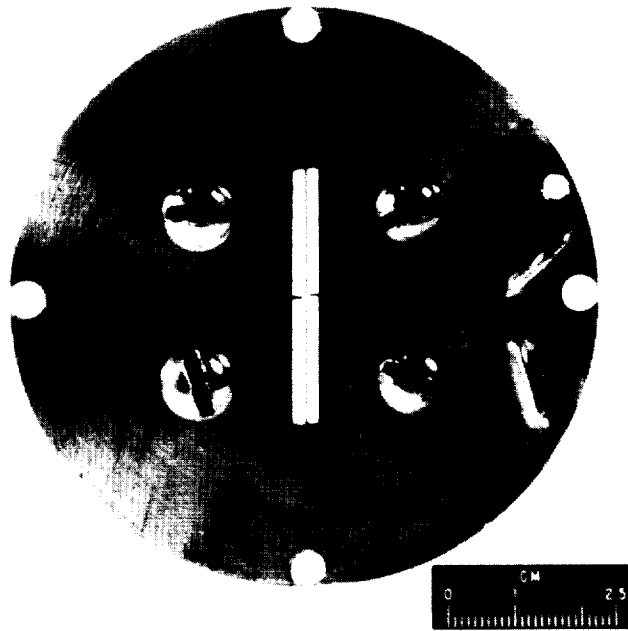
Figure 5. - Fuel element arrangement.

CD-9253



C-66-4114

(a) Holder disassembled.



C-66-4204

(b) View of upstream end.

Figure 6. - Test plate holder for cold-flow tests.

CONFIDENTIAL

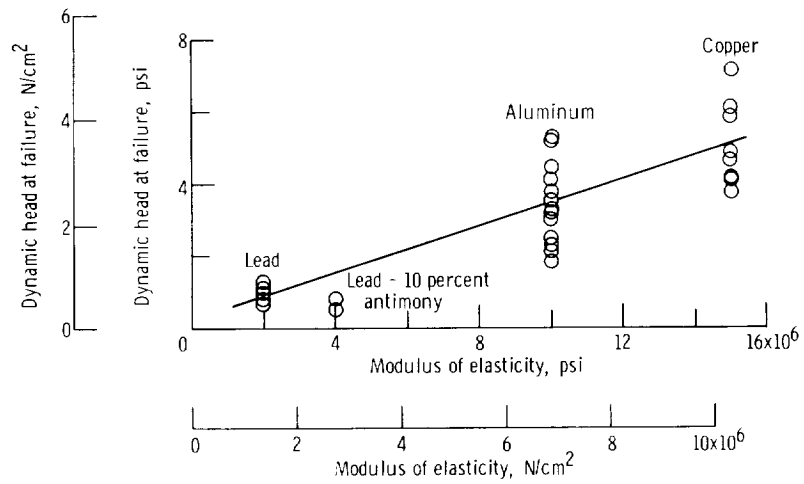


Figure 7. - Effect of modulus of elasticity on dynamic head at failure for plate. Plate dimensions, 2 by 2 by 0.020 inch (5.1 cm by 5.1 cm by 0.51 mm); flow channel height, 0.064 in. (1.625 mm); contact gap at upstream edge midspan, 0.010 in. (0.254 mm).

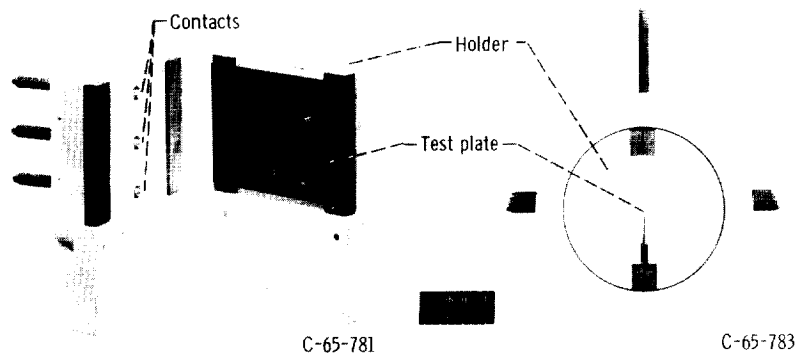


Figure 8. - Test-plate holder for hot-flow tests.

CONFIDENTIAL

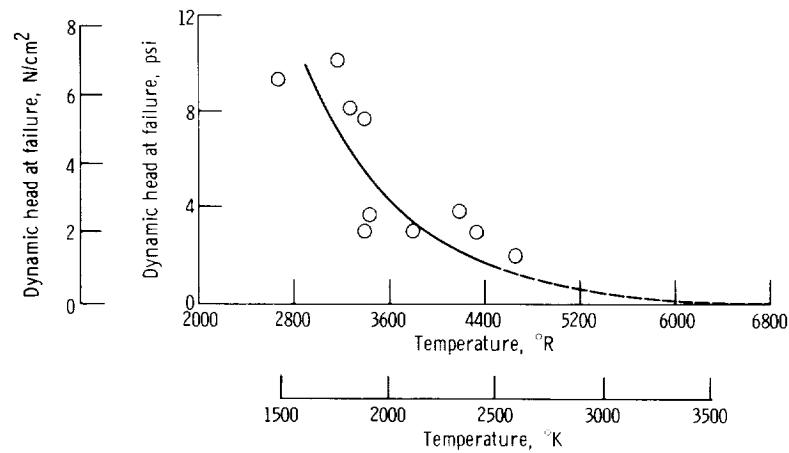
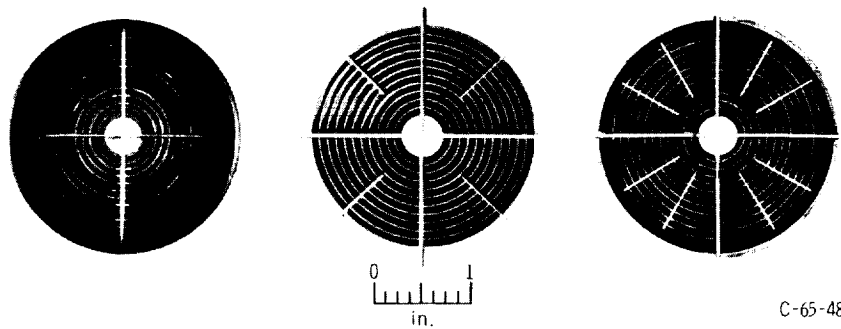


Figure 9. - Effect of temperature on dynamic head at failure for tungsten plate. Dimensions: unsupported span, 2.00 inches (5.08 cm); plate thickness, 0.02 inch (0.508 mm); plate to channel gap, 0.06 inch (1.524 mm); plate length in flow direction, 2.00 inches (5.08 cm).



C-65-487

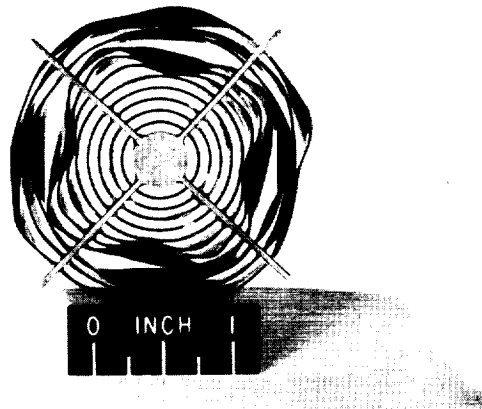
(a) Radial combs, 4; dynamic head at failure, 13 psi (8.96 N/cm²).

(b) Radial combs, 8; dynamic head at failure, 26 psi (17.9 N/cm²).

(c) Radial combs, 12; dynamic head at failure, 30 psi (20.7 N/cm²).

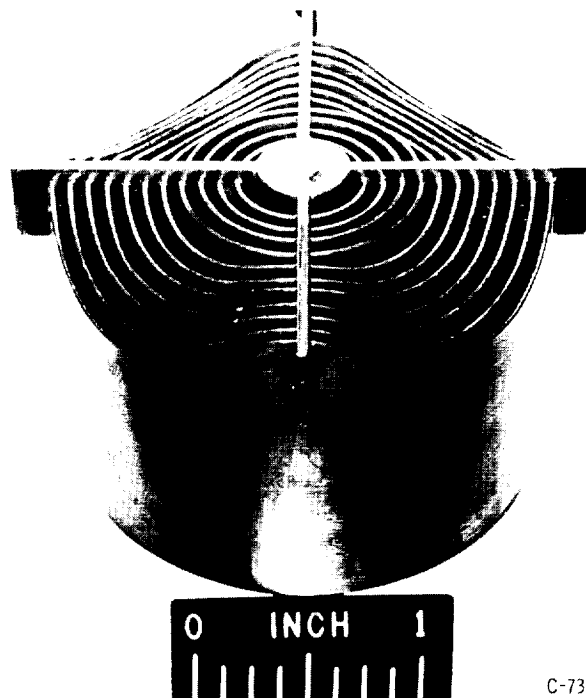
Figure 10. - Concentric ring elements of lead - 10 percent antimony.

~~CONFIDENTIAL~~



C-65612

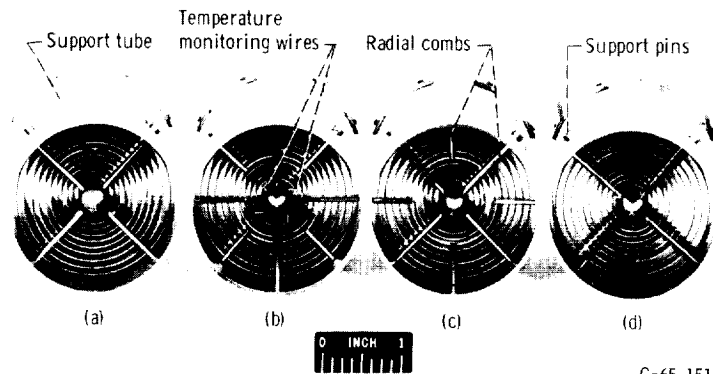
Figure 11. - Typical failure of concentric ring element.



C-73192

Figure 12. - Concentric ring element with scalloped upstream edges.

~~CONFIDENTIAL~~



C-65-1513

Figure 13. - Tungsten concentric cylinder elements prior to testing.

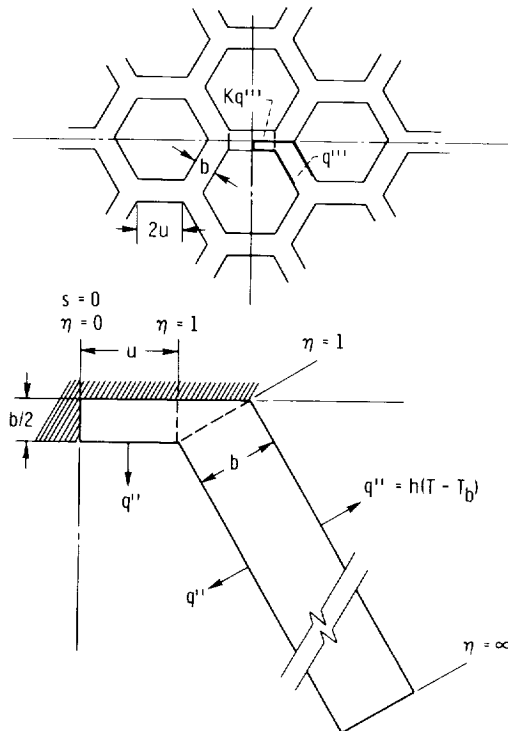


Figure 14. - Calculation model for local variation of heat-generation rates in honeycomb fuel-element configuration. Fueled material thickness, b ; heat-transfer coefficient, h ; ratio of heat-generation rates, K ; heat flux, q'' ; heat-generation rate per unit volume, q''' ; distance in direction of conductive heat flow, s ; temperature, T ; total bulk fluid temperature, T_b ; one-half width of web, u ; fractional distance, η .

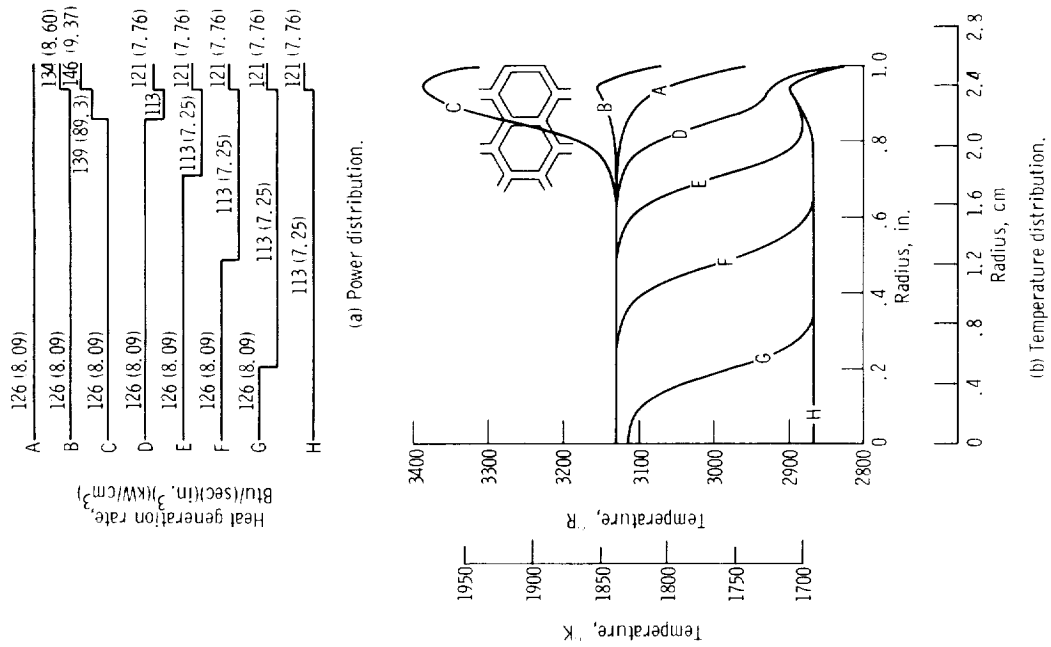


Figure 16. - Effect of radial power distribution on radial temperature profiles in honeycomb fuel-element stage at reactor inlet. Reference-design conditions.

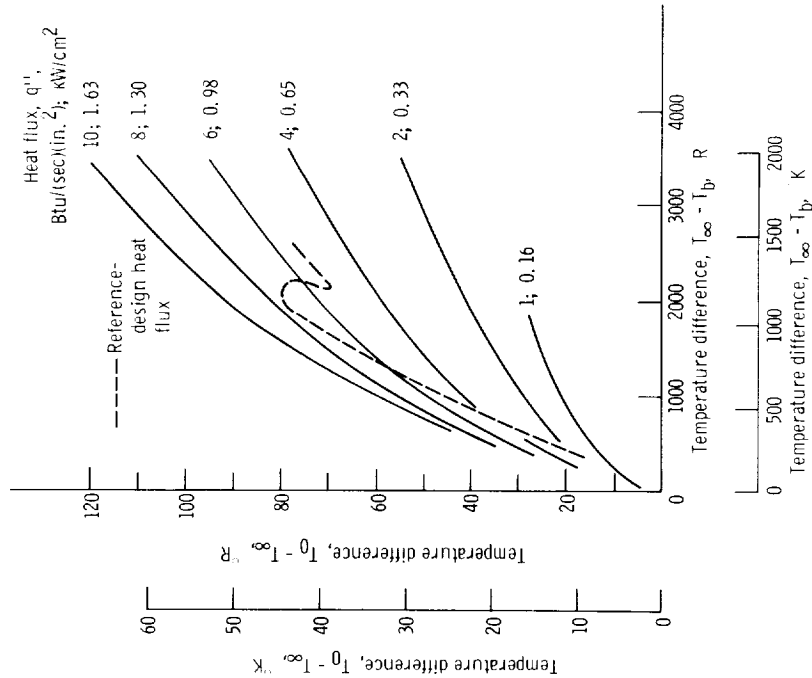


Figure 15. - Temperature difference due to one web operating at higher heat-generation rate. One-half width of web, 0.0361 inch (0.971 mm); fueled material thickness, 0.020 inch (0.502 mm); ratio of heat-generation rates, 1; 1; web thermal conductivity, 5.28×10^{-4} BTU/(sec.in. °R) (0.694 J/(sec.cm)(°K)).

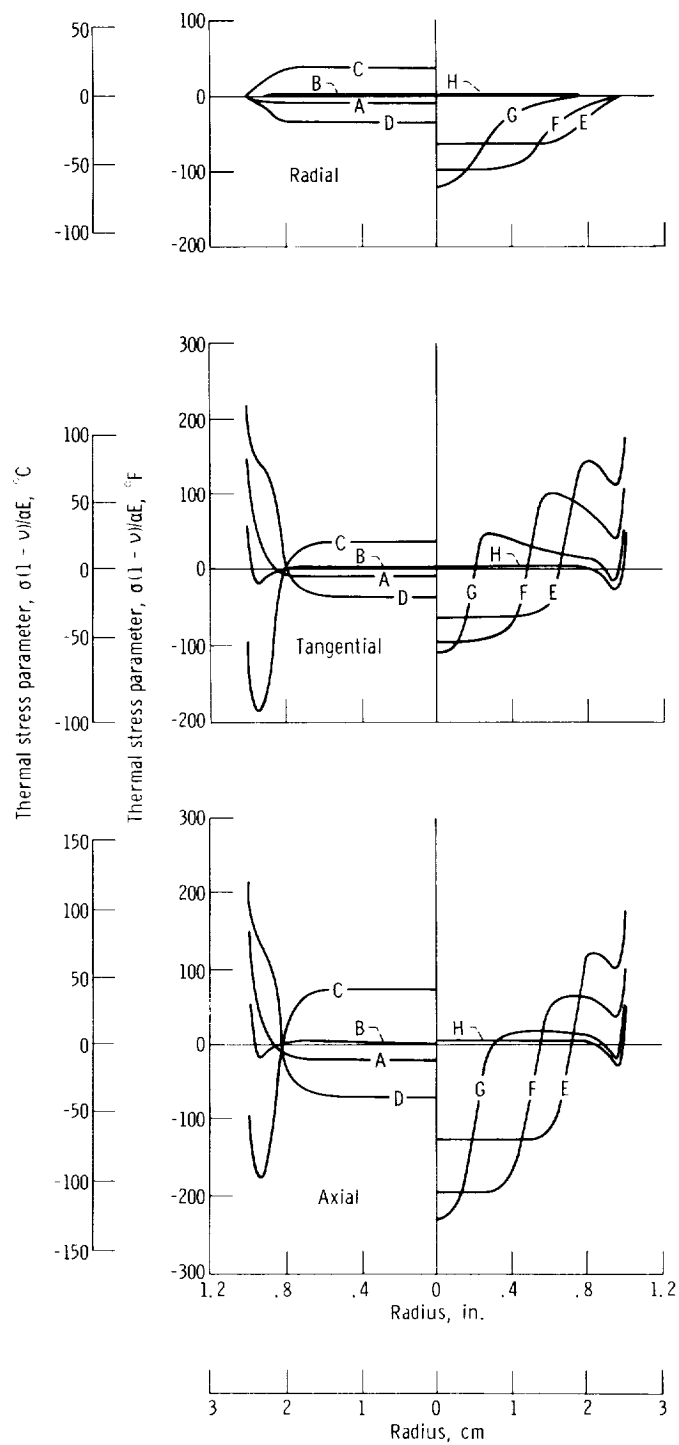
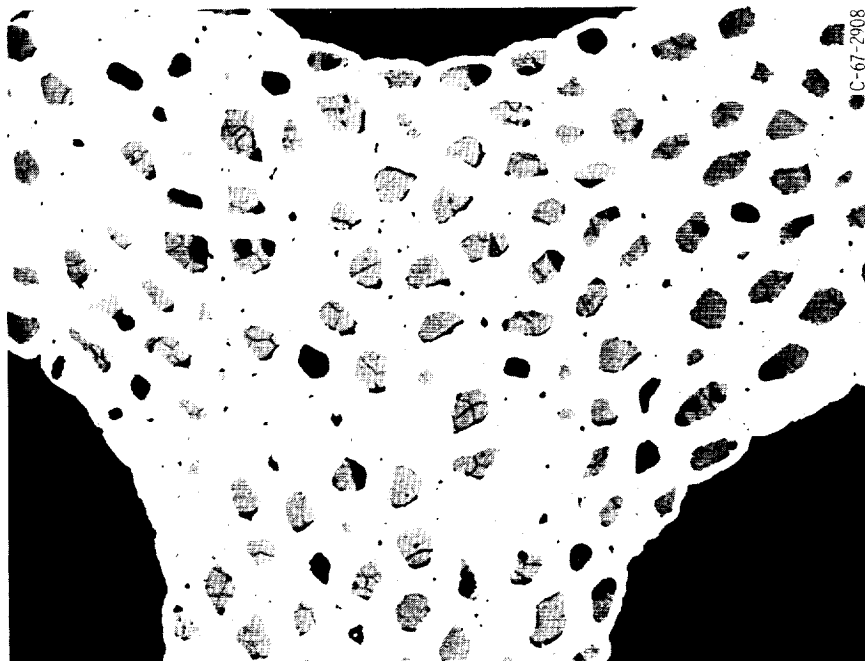
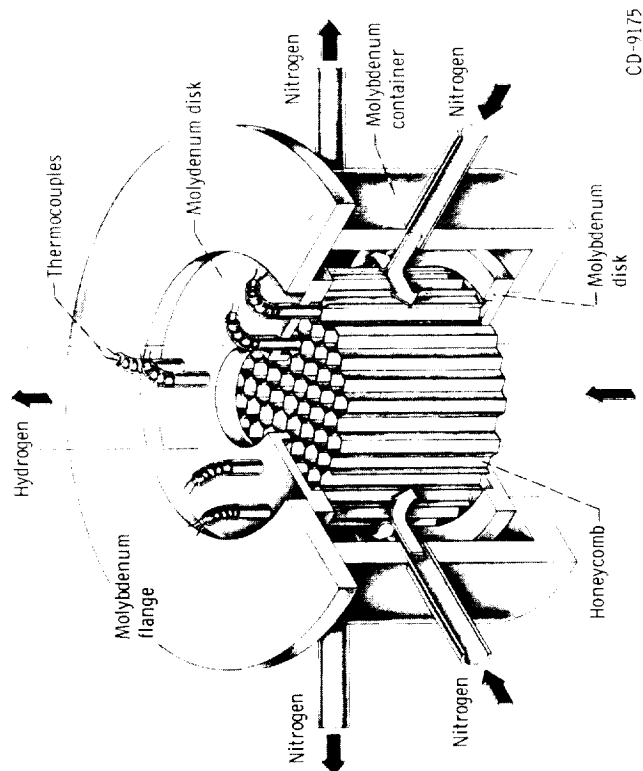


Figure 17. - Variation of thermal stress parameter with radius for temperature profiles of figure 16(b).



C-67-2908

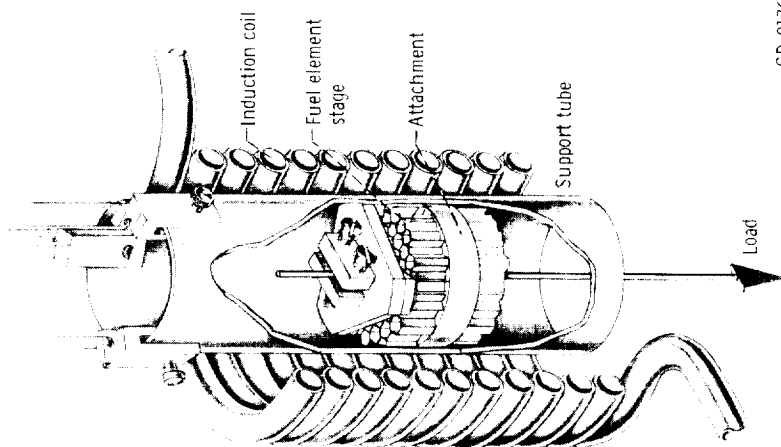
Figure 19. - Photomicrograph of honeycomb web section after thermal cycling.



CD-9175

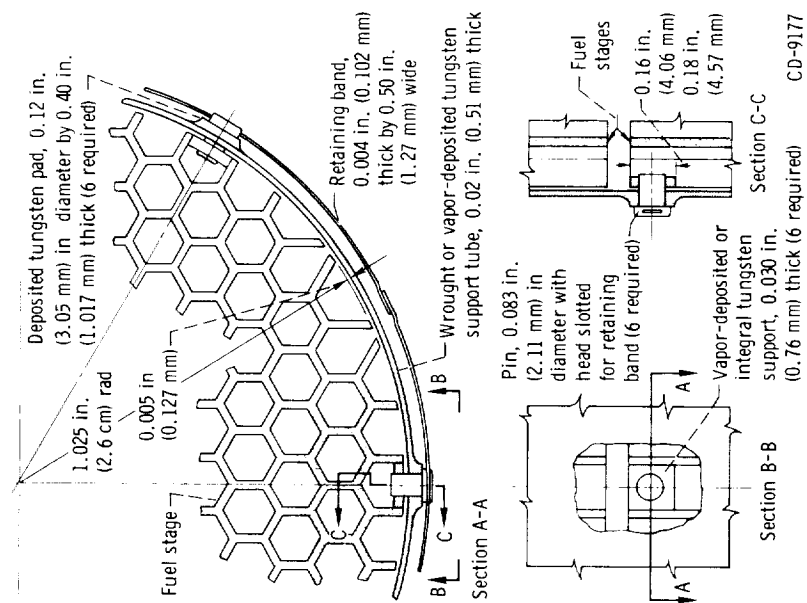
Figure 18. - Honeycomb thermal stress experiment.

CONFIDENTIAL



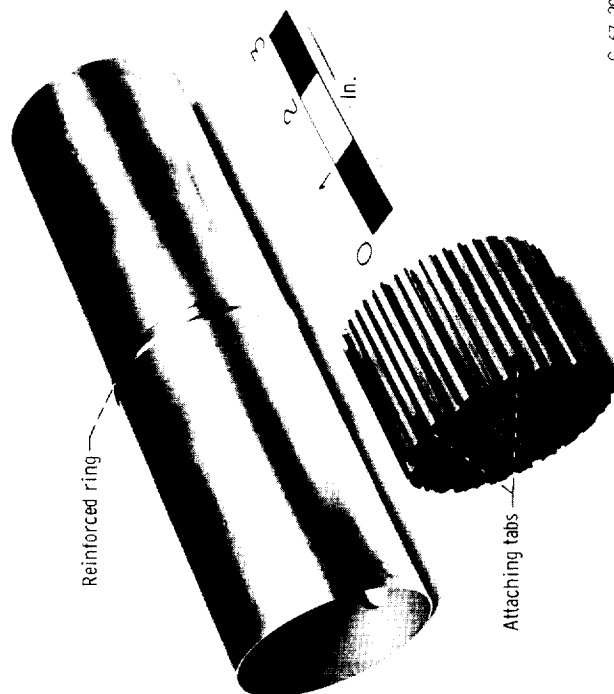
CD-9176

Figure 20. - Drawing of axial support test apparatus.



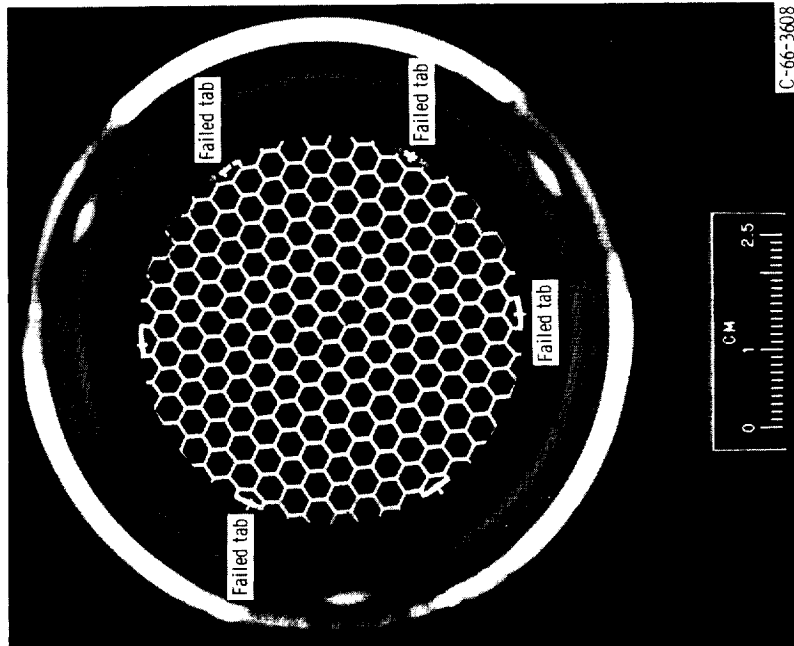
CD-9177

Figure 21. - Assembly of honeycomb and its housing using tabs and pins.



C-67-2909

Figure 22. - Support tube and honeycomb fuel stage for mechanical attachment.



C-66-3608

Figure 23. - Pin-tab mechanical attachment assembly after axial support test.

~~CONFIDENTIAL~~

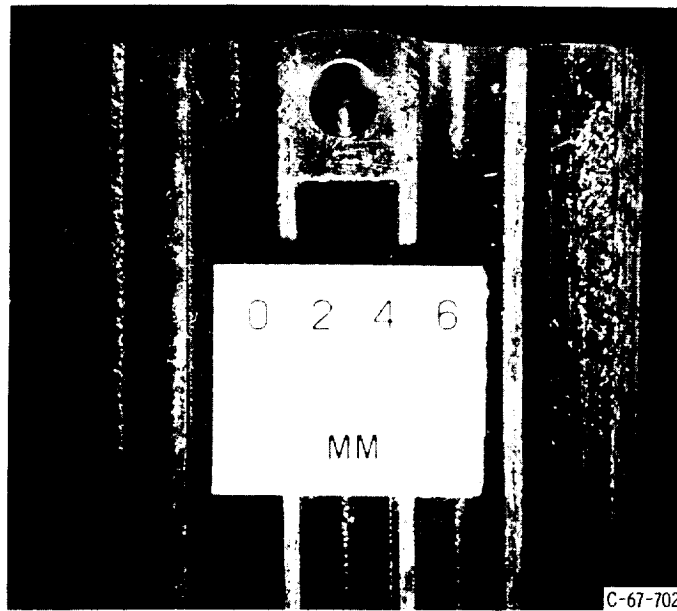


Figure 24. - Honeycomb fuel stage showing elongated tab hole after axial support test.

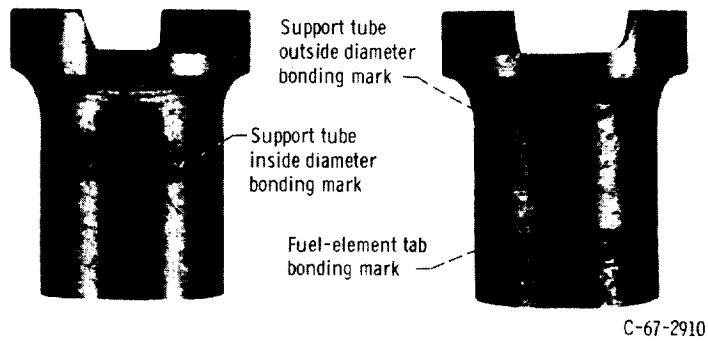


Figure 25. - Pin from mechanical attachment after axial support test.

~~CONFIDENTIAL~~

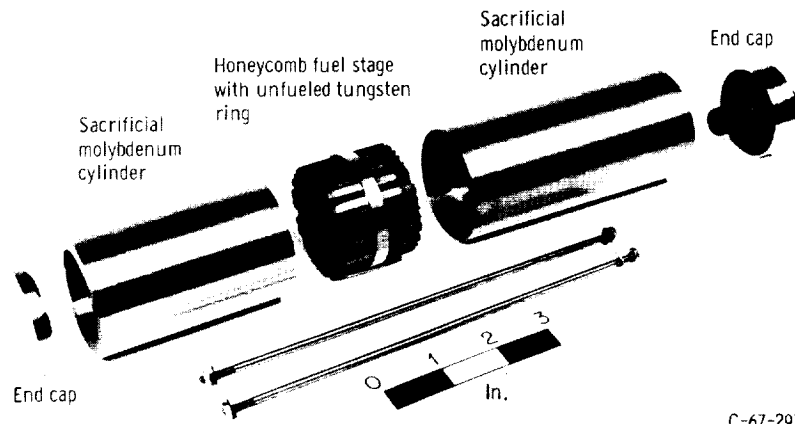


Figure 26. - Components for fuel-stage circumferential-ring metallurgical attachment.

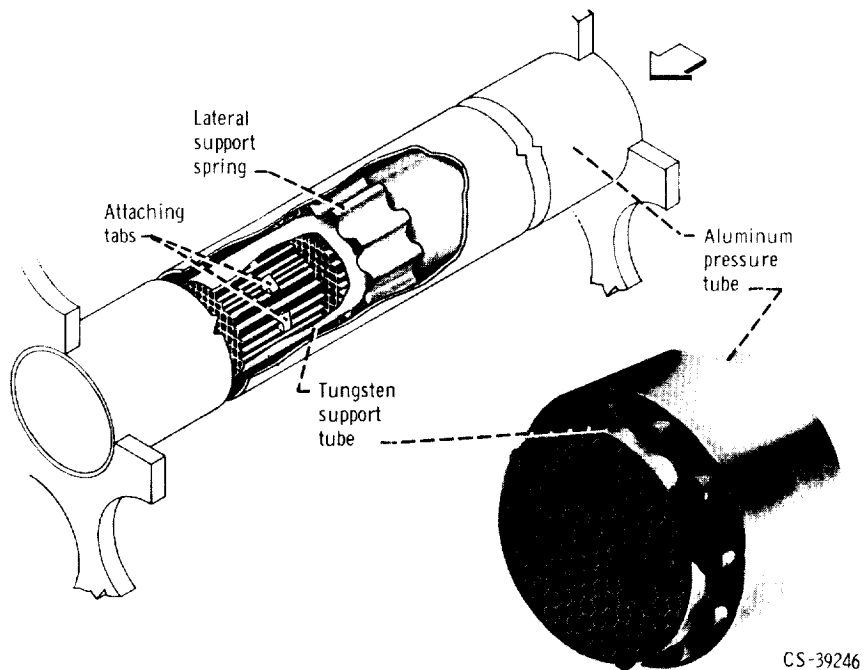


Figure 27. - Fuel-stage support using intermittent unfueled tungsten attaching tabs for metallurgical axial support.

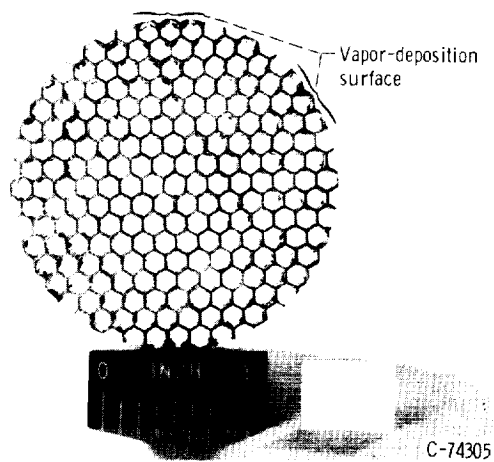


Figure 28. - Honeycomb fuel stage used for direct vapor-deposition attachment.

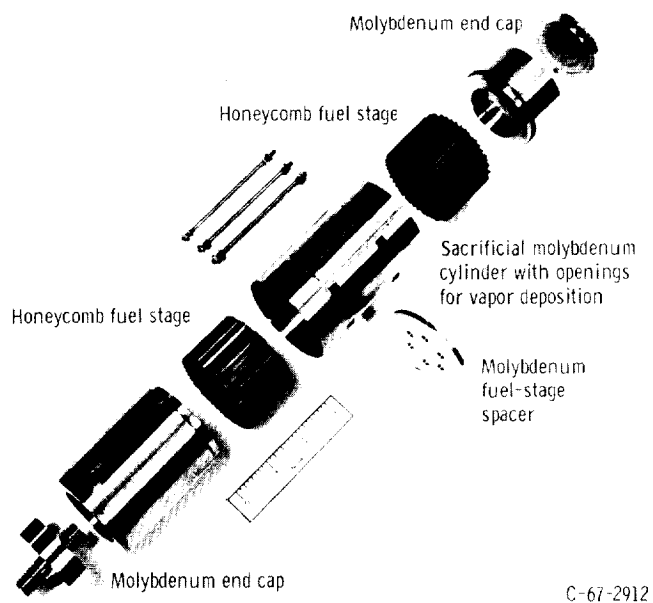
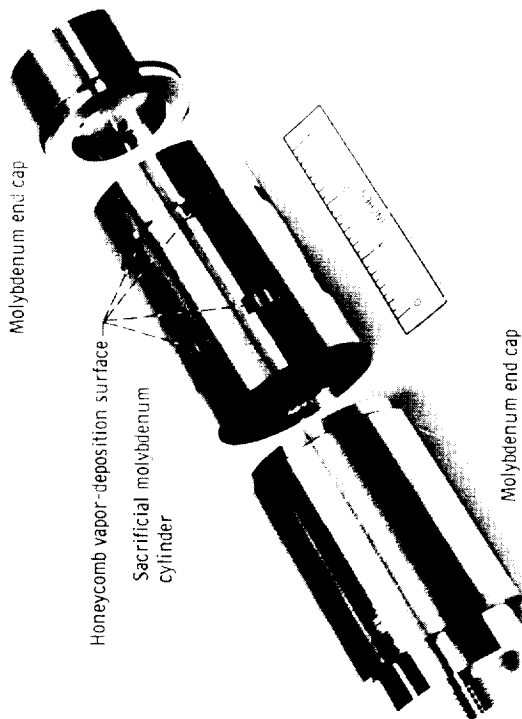
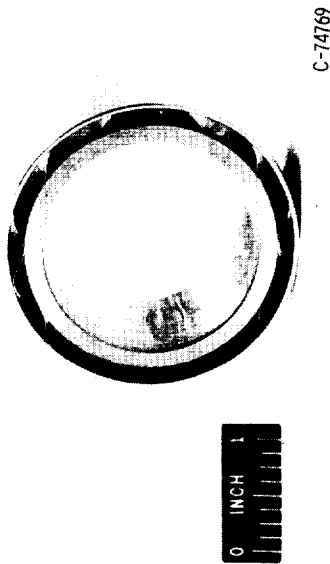


Figure 29. - Component layout for two-fuel stage subassembly with metallurgical attachment.



C-67-2913

Figure 30. - Partial assembly of two-fuel stages ready for metallurgical attachment.



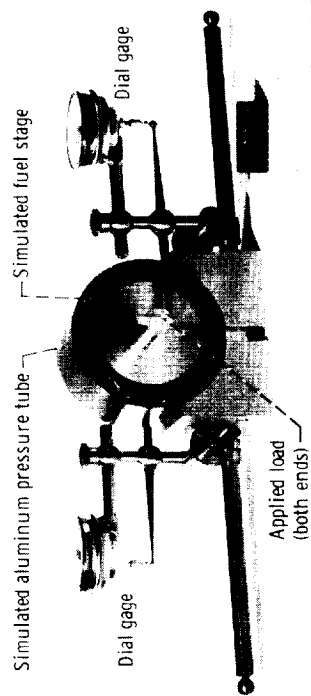
C-74769

Figure 31. - Relative thermal expansion test assembly. Tungsten outer ring (simulated aluminum pressure tube); 5-mil (0.127 mm) 12-lobe tungsten corrugation; tantalum inner ring (simulated fuel stage).



C-66-454

Figure 32. - Typical stapled joint of tungsten corrugation.



C-66-512

Figure 33. - Apparatus for static load-deflection measurement of corrugation.

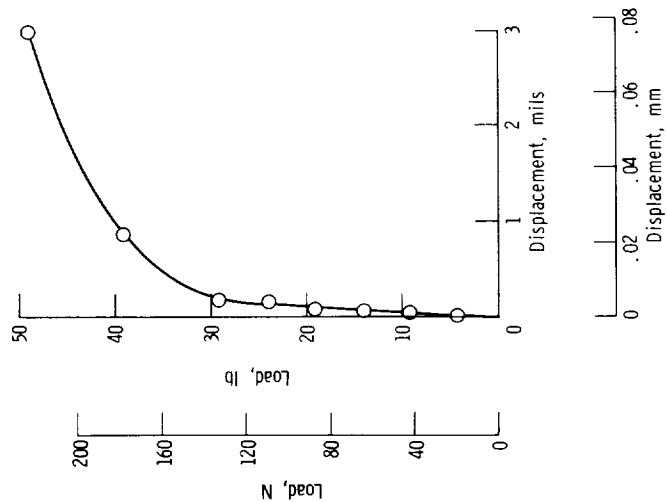
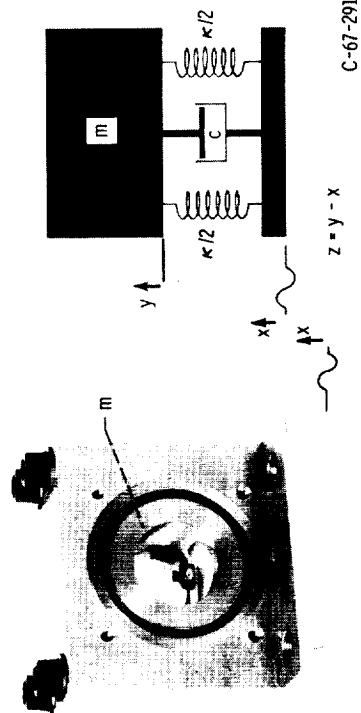


Figure 34. - Static load-deflection characteristics for a 5-mil thick (0.127 mm) 11-lobe tungsten corrugation 1.5 inches (3.81 cm) long.



C-67-2914

Figure 35. - Schematic model and vibration test components. Equivalent viscous damping coefficient, c ; spring constant, κ ; mass, m ; instantaneous table displacement, y ; instantaneous mass displacement, x ; instantaneous relative displacement, z .

~~CONFIDENTIAL~~

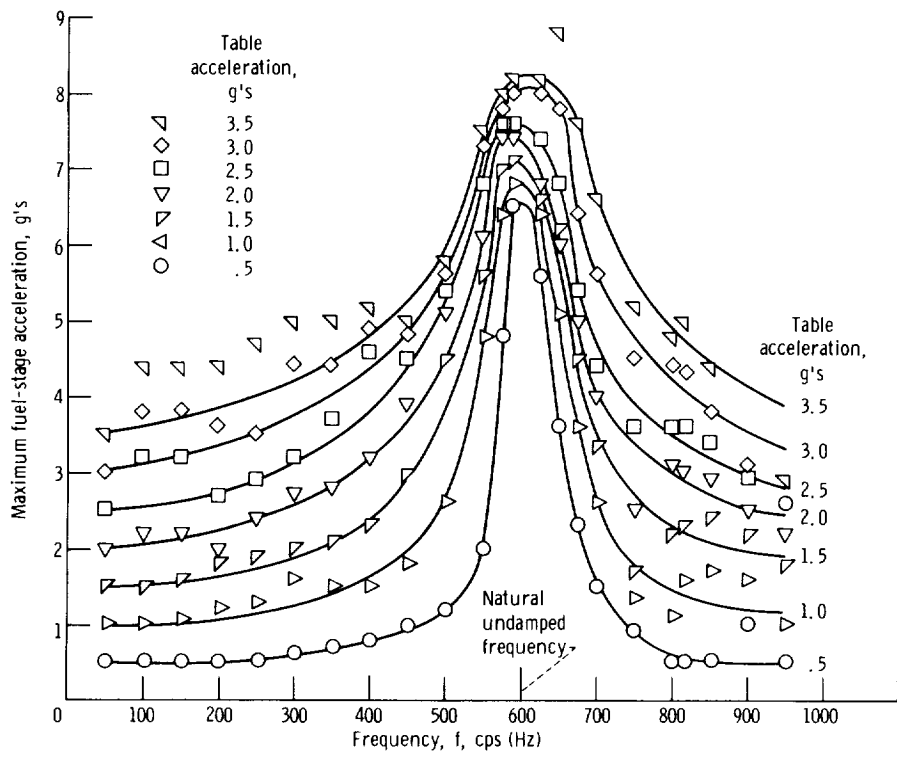


Figure 36. - Maximum fuel-stage acceleration as function of frequency for several table accelerations. Corrugation thickness, 3 mils (0.076 mm); length, 1.5 inches (3.81 cm); simulated fuel-stage mass, 1.1 pounds (0.50 kg).

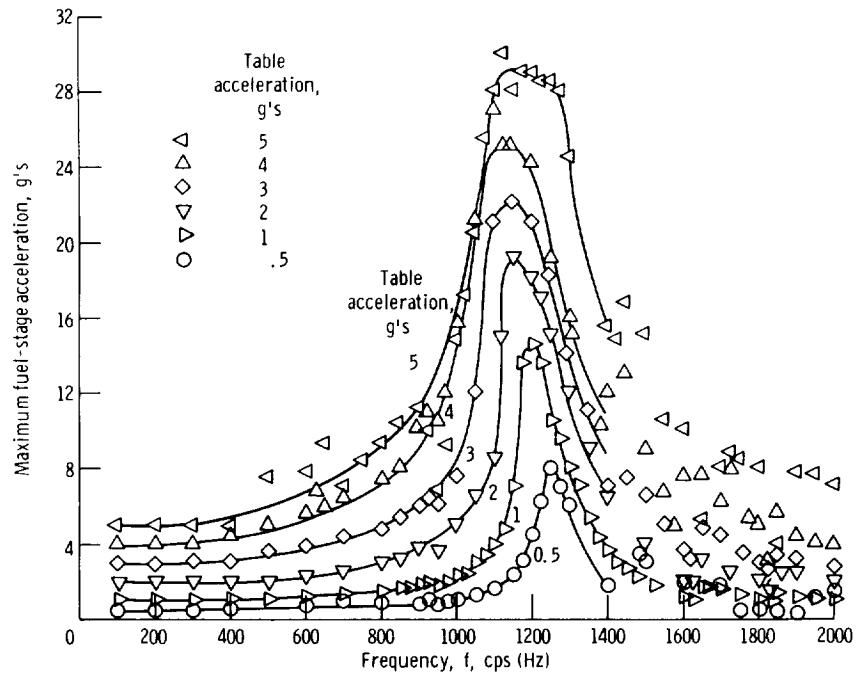
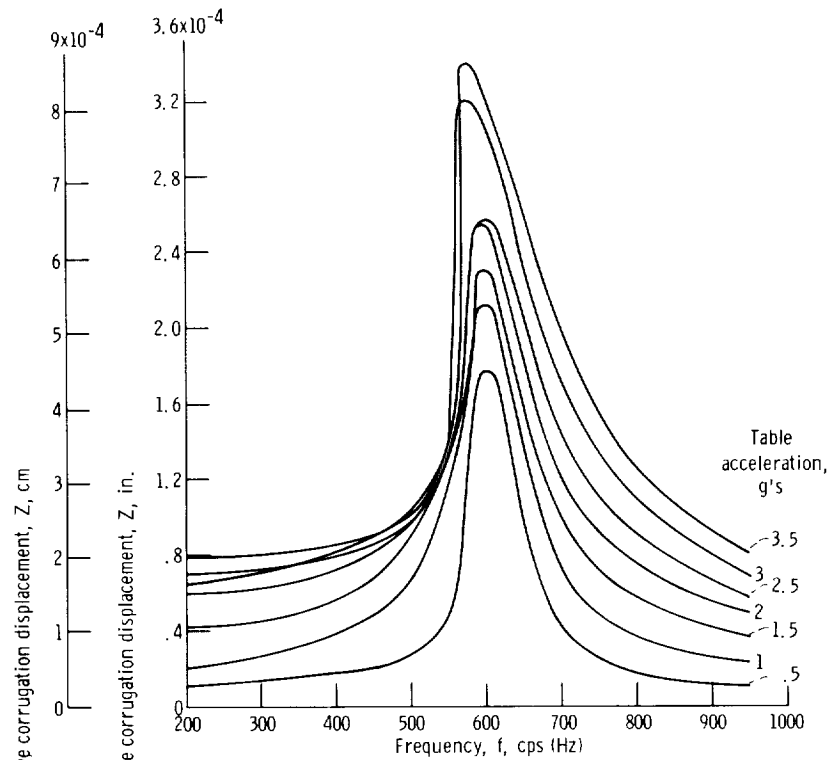
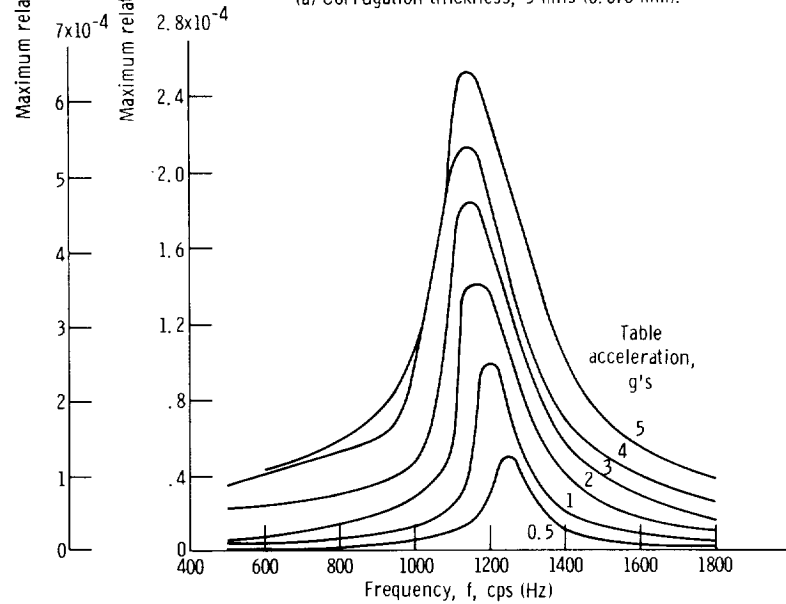


Figure 37. - Maximum fuel-stage acceleration as function of frequency for several table accelerations. Corrugation thickness, 5 mils (0.127 mm); length, 1.5 inches (3.81 cm); simulated fuel-stage mass, 1.1 pounds (0.50 kg).

~~CONFIDENTIAL~~



(a) Corrugation thickness, 3 mils (0.076 mm).



(b) Corrugation thickness, 5 mils (0.127 mm).

Figure 38. - Maximum relative corrugation displacement as function of frequency produced by constant table acceleration for each curve. Corrugation length, 1.5 inches (3.81 cm); number of lobes, 12; fuel-stage mass, 1.1 pounds (0.50 kg).

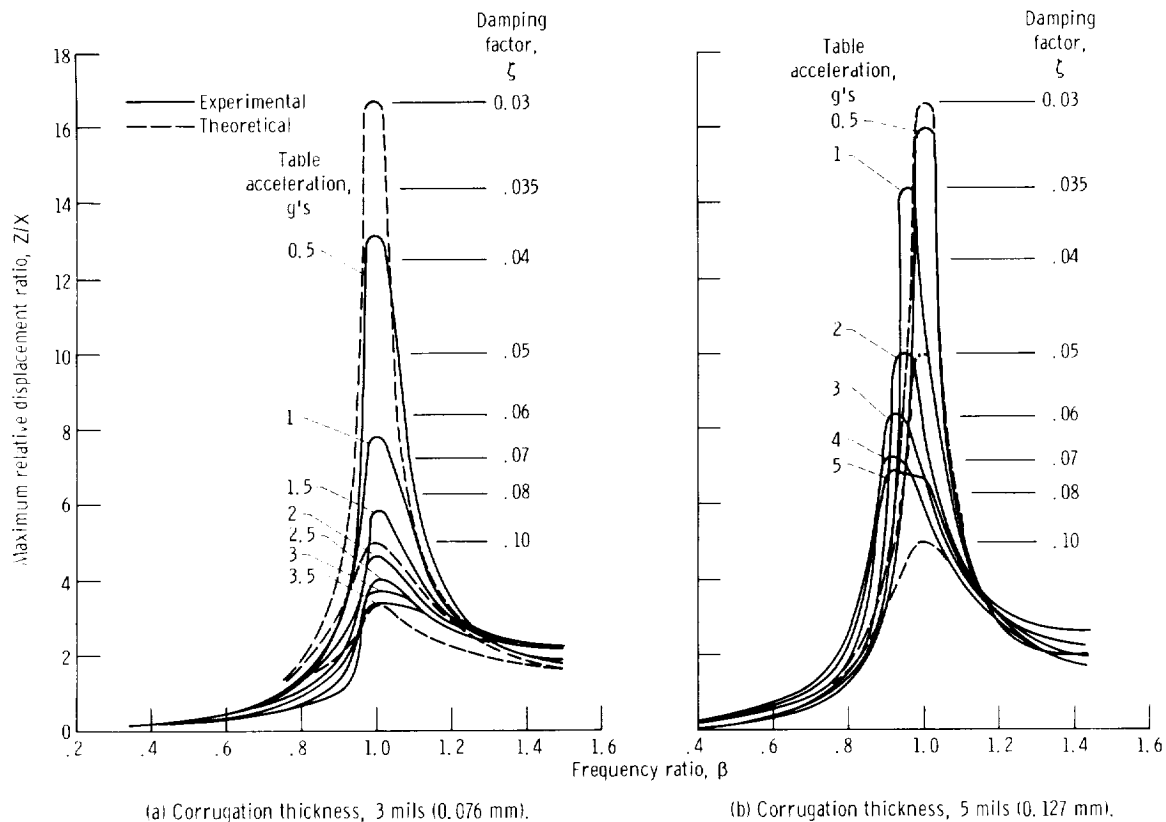


Figure 39. - Comparison of experimental and analytical curves for maximum relative displacement ratio as function of frequency ratio. Corrugation length, 1.5 inches (3.81 cm); number of lobes, 12; fuel-stage mass, 1.1 pounds (0.50 kg).

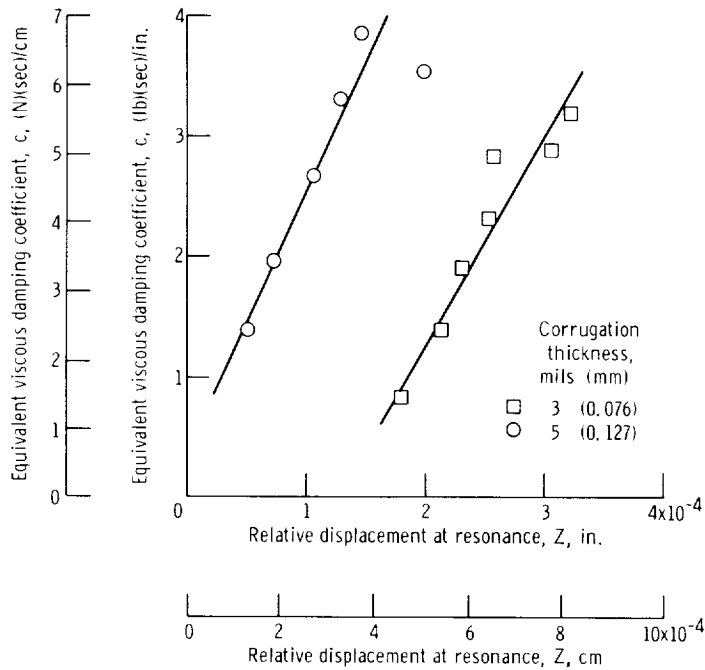


Figure 40. - Variation of equivalent viscous damping coefficient as function of relative displacement at resonance. Corrugation thickness, 3 mils (0.076 cm) and 5 mils (0.127 cm); number of corrugation lobes, 12.

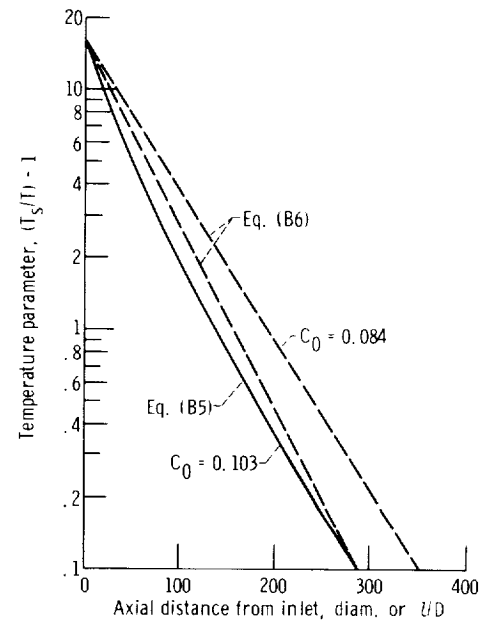


Figure 41. - Axial variations in propellant temperature.

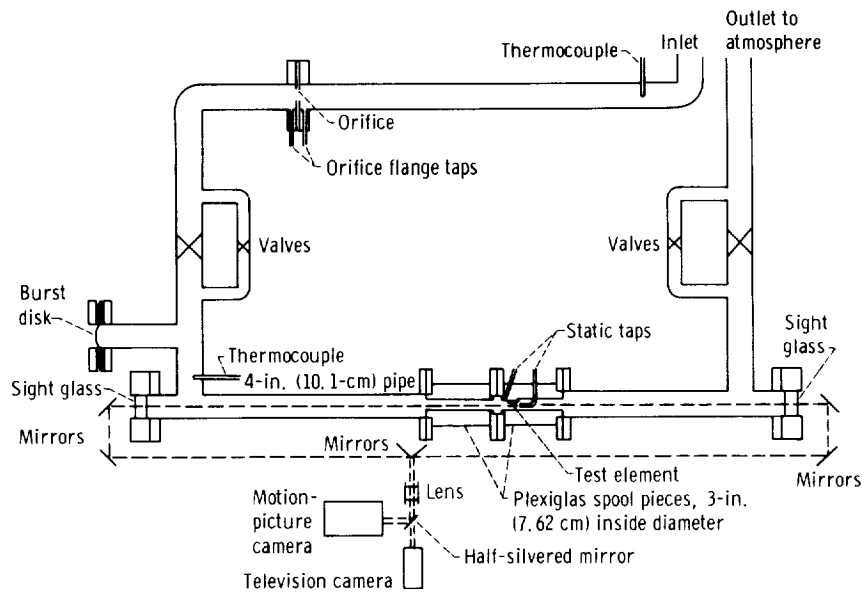


Figure 42. - Schematic diagram of test facility for cold-flow tests on simulated fuel elements.

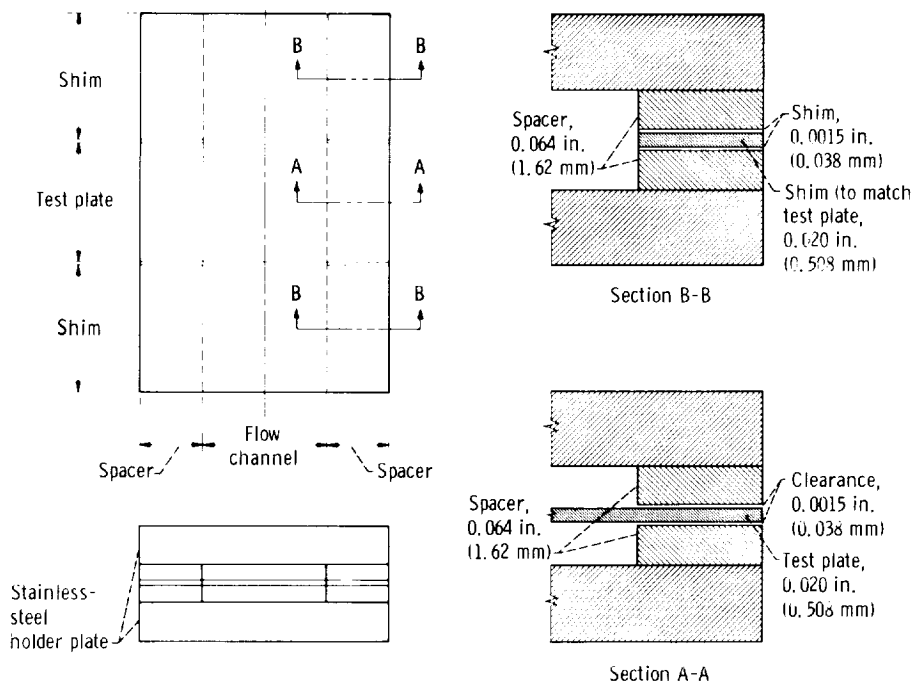


Figure 43. - Typical spacer arrangement for flat plate flow test.

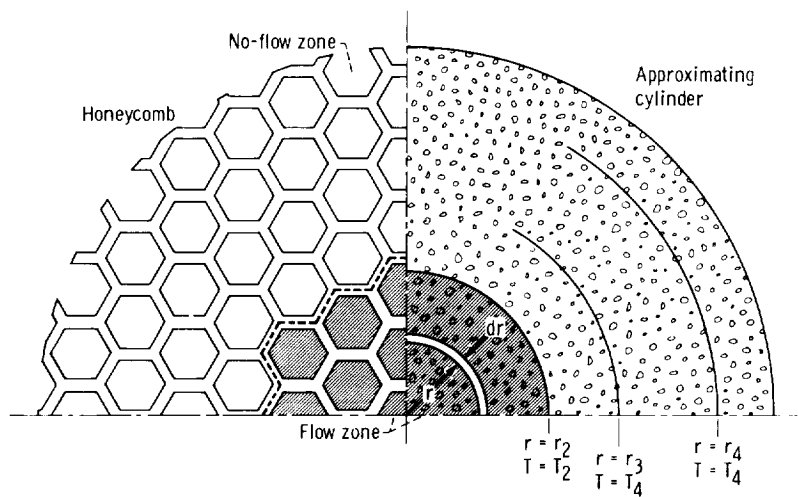


Figure 44. - Honeycomb and approximating cylinder. Radius, r ; temperature, T ; subscripts 2, 3, and 4 denote radial positions.

~~CONFIDENTIAL~~

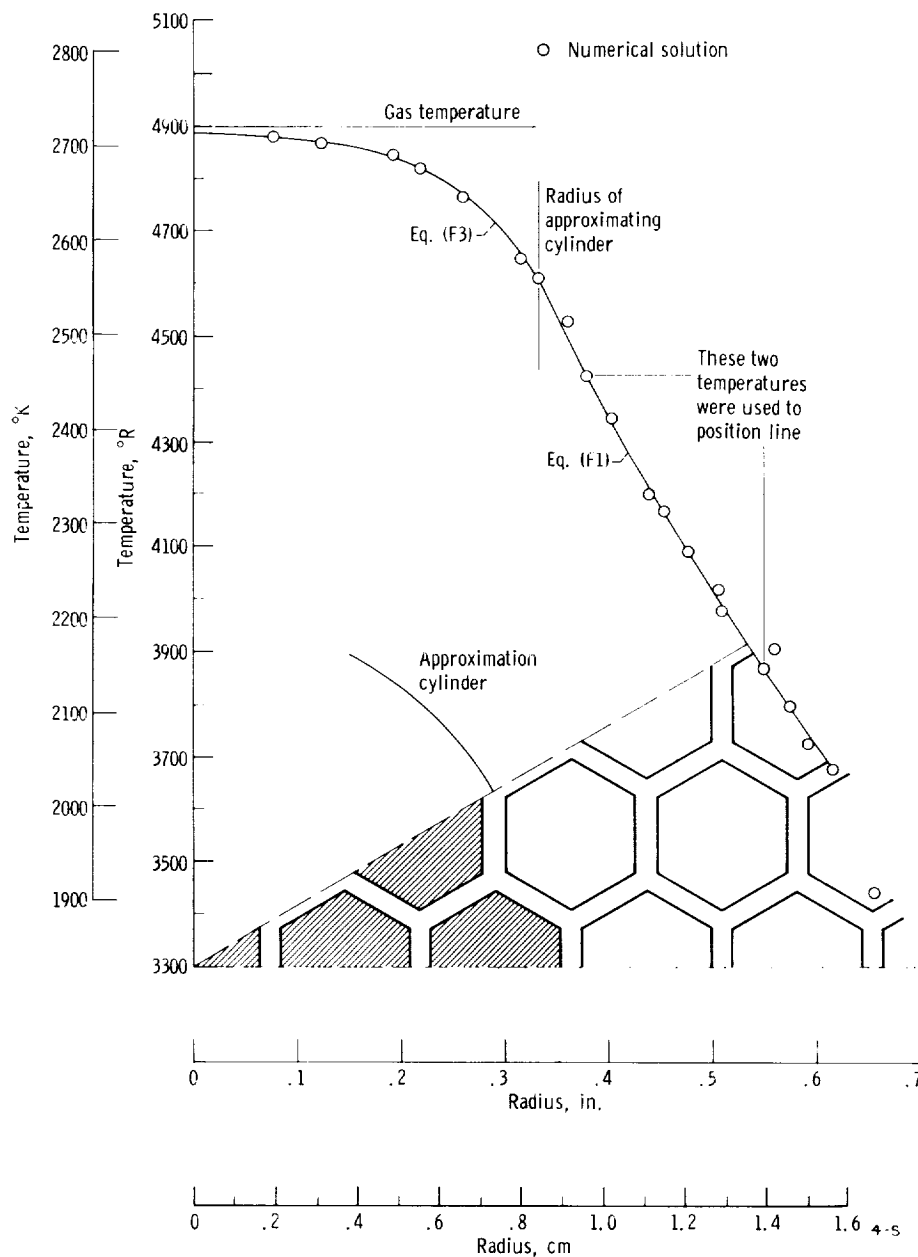


Figure 45. - Comparison of radial temperature profiles given by numerical honeycomb solution and homogenized cylinder solution.

~~CONFIDENTIAL~~